J. Fluid Mech. (2022), *vol*. 935, A39, doi:10.1017/jfm.2022.40

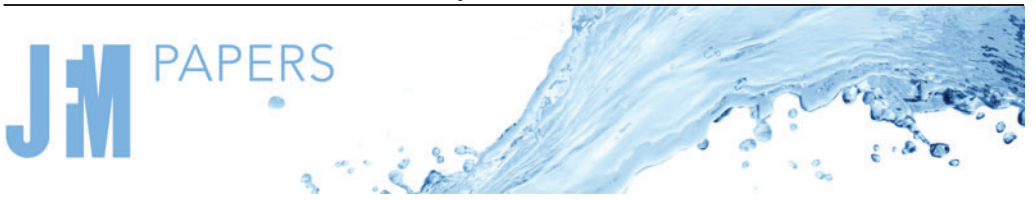

Swinging and tumbling of multicomponent vesicles in flow

Prerna Gera[1], **David Salac**[2] **and Saverio E. Spagnolie**[1,3,†]

[1]Department of Mathematics, University of Wisconsin-Madison, Madison, WI 53711, USA

[2]Department of Mechanical and Aerospace Engineering, University at Buffalo, Buffalo, NY 14260, USA

[3]Department of Chemical and Biological Engineering, University of Wisconsin-Madison, Madison, WI 53711, USA

(Received 21 August 2021; revised 30 December 2021; accepted 7 January 2022)

Biological membranes are host to proteins and molecules which may form domain-like structures resulting in spatially varying material properties. Vesicles with such heterogeneous membranes can exhibit intricate shapes at equilibrium and rich dynamics when placed into a flow. Under the assumption of small deformations and a two-dimensional system, we develop a reduced-order model to describe the fluid-structure interaction between a viscous background shear flow and an inextensible membrane with spatially varying bending stiffness and spontaneous curvature. Material property variations of a critical magnitude, relative to the flow rate and internal/external viscosity contrast, can set off a qualitative change in the vesicle dynamics. A membrane of nearly constant bending stiffness or spontaneous curvature undergoes a small amplitude swinging motion (which includes tangential tank-treading), while for large enough material variations the dynamics pass through a regime featuring tumbling and periodic phase-lagging of the membrane material, and ultimately for very large material variation to a rigid-body tumbling behaviour. Distinct differences are found for even and odd spatial modes of domain distribution. Full numerical simulations are used to probe the theoretical predictions, which appear valid even when studying substantially deformed membranes.

Key words: capsule/cell dynamics, flow-vessel interactions, membranes

1. Introduction

Biological membranes are often modelled as being homogeneous in composition, a simplification which has resulted in a trove of understanding of their shapes, dynamics in flows, fission and beyond. But real biological membranes contain a vast array of proteins which can form domains resulting in spatial variations in material properties, leading to changes in vesicle shapes (Seifert 1997; Hu, Weikl & Lipowsky 2011). Simpler systems

† Email address for correspondence: spagnolie@math.wisc.edu

of synthetic multicomponent vesicles, whose membranes can be composed of different lipid species, have been used to study the rich patterns and accompanying morphologies which emerge from elastic heterogeneity (Baumgart, Hess & Webb 2003; Veatch & Keller 2003). These findings have been corroborated and expanded upon using both numerical and analytical techniques (Elliott & Stinner 2013; Barrett, Garcke & Nürnberg 2017), which in turn are of use when attempting to infer membrane properties experimentally (Engelhardt, Duwe & Sackmann 1985; Baumgart *et al.* 2005; Tian *et al.* 2007).

The analytical study of vesicles with single-component membranes in flow has a long history. Keller & Skalak (1982) demonstrated with a two-dimensional elliptical membrane a transition from tank-treading (in which the membrane shape and orientation are fixed but the membrane material slides along the surface) to tumbling (the long axis rotates in a periodic fashion) beyond a critical interior/exterior viscosity contrast. But in general a vesicle is not ellipsoidal and its shape must be determined through a balance of interfacial forces, for instance, by describing the shape using a series expansion about small parameters such as excess area (Misbah 2006; Lebedev, Turitsyn & Vergeles 2007; Vlahovska & Gracia 2007). Detailed reviews on the small-deformation analyses for both vesicles and capsules are provided by Vlahovska (2015) and Vlahovska & Misbah (2019). Barthes-Biesel (1980), Barthes-Biesel & Rallison (1981) and Barthes-Biesel (1991) also considered the impact of the internal/external viscosity ratio for nearly spherical capsules assuming zero membrane bending stiffness. The leading-order solution demonstrates that in addition to tank-treading and tumbling behaviour as predicted by the Keller–Skalak model, there is another mode called 'swinging' (Noguchi & Gompper 2007), 'vacillating breathing' (Misbah 2006) or 'trembling' (Kantsler & Steinberg 2006; Lebedev, Turitsyn & Vergeles 2008) in which the orientation of the major axis oscillates while the vesicle undergoes significant deformations – see also the review by Lebedev *et al.* (2008). Some of the above terms are used interchangeably by various authors, a semantic issue also noted by Misbah (2012).

Phase diagrams for the shapes and dynamics of vesicles in linear flows have been mapped out by numerous authors (Lebedev *et al.* 2008; Deschamps *et al.* 2009*a*; Deschamps, Kantsler & Steinberg 2009*b*; Zhao & Shaqfeh 2011; Zabusky *et al.* 2011; Abreu *et al.* 2014); see also Barthes-Biesel (2016). The roles of nearby boundaries (Zhao, Spann & Shaqfeh 2011), inertia (Salac & Miksis 2012), semi-permeability (Quaife, Gannon & Young 2021), enclosed particles (Veerapaneni *et al.* 2011*b*), fluid viscoelasticity (Mushenheim *et al.* 2016; Seol *et al.* 2019), thermal fluctuations (Wortis, Jarić & Seifert 1997; Schneider, Jenkins & Webb 1984; Morse & Milner 1994; Michalet, Bensimon & Fourcade 1994; Seifert 1999; Finken *et al.* 2008; Ahmadpoor & Sharma 2016) and active internal stresses (Gao & Li 2017; Young, Shelley & Stein 2021) are among the many additional physical and biological features that have been considered, and a large body of literature is devoted to suspensions of many deformable particles such as cells and vesicles in flows (Kantsler, Segre & Steinberg 2008; Vlahovska, Podgorski & Misbah 2009; Veerapaneni *et al.* 2011*a*; Zhao, Shaqfeh & Narsimhan 2012; Freund 2014; Kumar & Graham 2015; Raffiee, Dabiri & Ardekani 2019).

The behaviours of multicomponent vesicles in flows, meanwhile, has only just begun to attract attention. Analytical results are scarce but numerical simulations have offered substantial insight. Simulations in a stationary environment have revealed wrinkling and budding deformations (Li, Lowengrub & Voigt 2012) and the formation of multicomponent vesicles by adhesion and fusion (Zhao & Du 2011). Sohn *et al.* (2010) studied two-dimensional multicomponent vesicles in a background shear flow, along with the evolution of distinct surface phases, finding highly complex morphologies and dynamics for highly deformed vesicles. Smith & Uspal (2007) showed using dissipative

particle dynamics simulations that a shear flow can be used to separate buds from a multicomponent vesicle. The influence of both bending rigidity and spontaneous curvature variation on the equilibrium shape of a vesicle has also been investigated (Cox & Lowengrub 2015). Subsequent boundary integral simulations by Liu *et al.* (2017) showed a transition from tumbling to tank-treading to 'phase-treading' of the constituents along the surface upon increasing the shear rate. Analytic results have also shown that a variation of bending rigidity along a surface can induce migration in tank-treading vesicles (Olla 2011). Synthetic systems have also been fruitful for testing theoretical predictions. Experiments using a two-phase lipid vesicle in such a flow as a simplified model of red blood cell dynamics showed similarly complex features (Tusch *et al.* 2018). Gera & Salac (2018*b*) then used simulations to probe a wide array of morphological changes due to spatially varying bending stiffness and line tension between two lipid phases. The phase separation process itself is naturally of great interest, and experiments have been used to study spinodal decomposition and viscous fingering along membrane surfaces (Veatch & Keller 2003; Lowengrub, Rätz & Voigt 2009; Marenduzzo & Orlandini 2013; Stanich *et al.* 2013).

In this article we derive analytical predictions for a two-dimensional, multicomponent vesicle in a shear flow under the assumption of small deformations and already-formed domains. Among the fruits of the reduced-order model so produced is a single equation describing the inclination angle dynamics when the distribution of material properties varies in the second spatial mode, the frequency in which they interact most strongly with the extensional part of the background flow. In this most dynamic case, a change in behaviour from swinging with tank-treading to tumbling is identified, passing through a transition regime with periodic phase-lagging of the material relative to the vesicle's elongated axis. The method of matched asymptotics is used to produce an approximate solution to the inclination angle equation through this sharp transition, as well as the critical value of the bifurcation parameter signalling the transition from swinging to tumbling which depends on the material property gradient, shear rate and internal/external viscosity contrast. The asymptotic predictions are shown to compare favourably to the results of full numerical simulations, even for highly deformed vesicles.

The paper is organized as follows. After presenting the mathematical framework in § 2 to describe the coupling of the fluid flow and elastic membrane stresses at zero Reynolds number (Stokes flow), an expansion is performed around a nearly circular vesicle to reduce the system down to time-dependent shape equations. The classical case of constant membrane material properties is presented in § 3, in which the results of asymptotic predictions are compared to full numerical simulations. In § 4 attention is turned to the case of interest, that of spatially varying material properties, in which the resulting dynamics is shown to depend strongly on the spectrum of the material properties, and in particular the parity of the number of domains. Concluding remarks are provided in § 5.

2. Mathematical model

2.1. *Membrane shape and small deformations*

The membrane, or vesicle surface, S, is described by a surface parameterization $\boldsymbol{r}(s, t)$, where s is the arclength and t is time. The unit tangent and outward-pointing normal vectors on the surface are written as $\hat{\boldsymbol{s}} = \boldsymbol{r}_s$ and $\hat{\boldsymbol{n}} = \hat{\boldsymbol{s}}^{\perp}$. The membrane is assumed area-preserving with area A and inextensible with length $L = 2\pi a$ (so that $s \in [0, L)$), where a is the characteristic radius.

In the event that the membrane area is not far removed from that of a circle of length L, it becomes convenient to work in polar coordinates (r, θ), with unit vectors $\hat{\boldsymbol{r}}$ and $\hat{\boldsymbol{\theta}}$, and we

represent the surface S as $\boldsymbol{r}(s(\theta,t),t) = r(\theta,t)\hat{\boldsymbol{r}}(\theta) = a(1+\varepsilon\rho(\theta,t)+\varepsilon^2\rho^{(2)}(\theta,t))\hat{\boldsymbol{r}}(\theta)$, where ε is a small non-negative constant. For small ε we have $\hat{\boldsymbol{s}} = \hat{\boldsymbol{\theta}} + \varepsilon\rho_\theta\hat{\boldsymbol{r}} + O(\varepsilon^2)$ and $\hat{\boldsymbol{n}} = \hat{\boldsymbol{r}} - \varepsilon\rho_\theta\hat{\boldsymbol{\theta}} + O(\varepsilon^2)$. A schematic is provided in figure 1. Fourier series representations of the shape functions ρ and $\rho^{(2)}$ are given by

$$\rho(\theta,t) = \sum_{n=0}^{\infty} a_n(t)\cos(n\theta) + b_n(t)\sin(n\theta), \tag{2.1}$$

where $a_n(t)$ and $b_n(t)$ are the time-varying Fourier coefficients, with a similar expression for $\rho^{(2)}(\theta,t)$ with coefficients $a_n^{(2)}(t)$ and $b_n^{(2)}(t)$. The length of the membrane may then be written (suppressing the time dependence for the sake of presentation), for $\varepsilon \ll 1$ as

$$L = \int_0^{2\pi} |\boldsymbol{r}_\theta|\,\mathrm{d}\theta = 2\pi a\left(1+\varepsilon a_0+\varepsilon^2 a_0^{(2)}\right) + \frac{\pi a\varepsilon^2}{2}\sum_{n=1}^{\infty} n^2\left(a_n^2+b_n^2\right) + O(\varepsilon^3). \tag{2.2}$$

Fixing the membrane length to $2\pi a$ thus requires that $a_0 = 0$ and

$$a_0^{(2)} = -\sum_{n=1}^{\infty}\frac{n^2}{4}\left(a_n^2+b_n^2\right), \tag{2.3}$$

and the enclosed area may in that case be written as

$$A = \int_0^{2\pi}\frac{r^2}{2}\mathrm{d}\theta = \pi a^2\left(1-\frac{\varepsilon^2}{2}\sum_{n=1}^{\infty}\left(n^2-1\right)\left({a_n}^2+{b_n}^2\right)\right) + O(\varepsilon^3). \tag{2.4}$$

The constant ε may be written in terms of the area enclosed by the membrane if desired as $\varepsilon = (2/3)^{1/2}(1-R_A)^{1/2}/Q$, where $R_A = A/(\pi a^2)$ is the 'reduced area' (equal to unity when the membrane is circular) and

$$Q = \left(\tfrac{1}{3}\sum_{n=1}^{\infty}(n^2-1)({a_n}^2+{b_n}^2)\right)^{1/2}. \tag{2.5}$$

The value of Q must be constant in time if the dynamics is area-preserving. The Fourier contributions at mode $n=1$ correspond to translation of the vesicle without shape change up to $O(\varepsilon^3)$, and hence do not contribute in the expression above.

2.2. *Stokes equations and viscous traction*

The incompressible Stokes equations describing viscous flow both outside (+) and inside (−) the vesicle are given by

$$\nabla\cdot\boldsymbol{\sigma}^{\pm} = \boldsymbol{0}, \quad \nabla\cdot\boldsymbol{u} = 0, \tag{2.6a,b}$$

where $\boldsymbol{u}(\boldsymbol{x},t)$ is the fluid velocity a point $\boldsymbol{x}=(x,y)$ at time t and $\boldsymbol{\sigma}^{\pm} = -p^{\pm}\boldsymbol{I} + \mu^{\pm}(\nabla\boldsymbol{u}^{\pm} + \nabla^T\boldsymbol{u}^{\pm})$ are the Newtonian stress-tensors for each fluid domain, with $p^{\pm}$ and $\mu^{\pm}$ the pressures and fluid viscosities external and internal to the membrane. The undisturbed background flow is a linear, horizontal shear flow with shear rate $\dot{\gamma}$, $\boldsymbol{u} = \dot{\gamma}y\hat{\boldsymbol{x}}$, with constant pressure p_∞. A no-slip boundary condition is assumed between the fluid and membrane velocities on both sides of the membrane (there is no relative slipping between

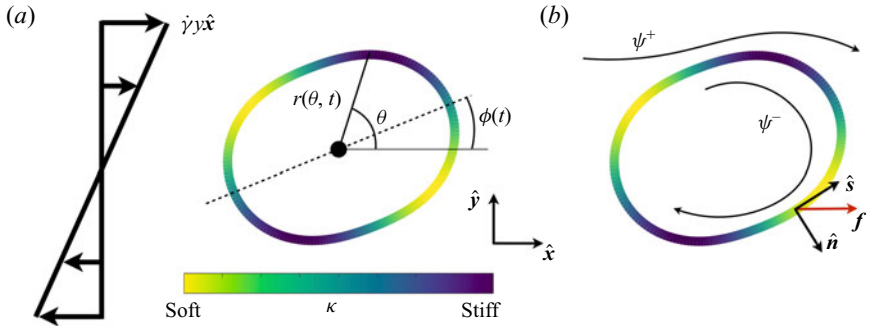

Figure 1. (*a*) Schematic of the two-dimensional inextensible membrane with spatially varying bending stiffness (or spontaneous curvature) in a shear flow, $\dot{\gamma}y\hat{\boldsymbol{x}}$; κ denotes the spatial variation in bending stiffness in (2.14*a*,*b*). Softer regions are lighter in colour than the darker, stiffer domains. Here the material properties vary in the second spatial mode (e.g. the membrane has two stiffer domains). (*b*) The stream function for the external and internal flows are denoted by ψ^+ and ψ^-, respectively; the viscous traction, $\boldsymbol{f}$, in (2.7), instantaneously balances the elastic traction in (2.12).

the inner and outer membrane surfaces). The local viscous tractions, $\boldsymbol{f}^{\pm} = \pm\hat{\boldsymbol{n}} \cdot \boldsymbol{\sigma}^{\pm}$, acting on the membrane from the exterior and interior interfaces result in the combined local viscous traction

$$\boldsymbol{f} = \hat{\boldsymbol{n}} \cdot [\boldsymbol{\sigma}]_S = -[p]_S\hat{\boldsymbol{n}} + \hat{\boldsymbol{n}} \cdot \Big[\mu(\boldsymbol{\nabla u} + \boldsymbol{\nabla}^T\boldsymbol{u})\Big]_S, \tag{2.7}$$

with $[f]_S = (f^+ - f^-)|_S$ defined to be the jump in f across the boundary S.

The continuity equation in the bulk fluid is immediately satisfied with the introduction of a stream function, ψ, defined such that $\boldsymbol{u} = \boldsymbol{\nabla}^{\perp}\psi = \psi_y\hat{\boldsymbol{x}} - \psi_x\hat{\boldsymbol{y}}$. The Stokes equations then reduce to biharmonic equations interior and exterior to the membrane:

$$\nabla^4\psi^{\pm} = 0, \tag{2.8}$$

with $\psi^+ \to \dot{\gamma}y^2/2$ as $|\boldsymbol{x}| \to \infty$, the background shear flow. The general form of the θ-periodic solution to the biharmonic equation is given in Appendix A. Continuity of velocity across the membrane boundary demands that

$$[\boldsymbol{\nabla}\psi]_S = \boldsymbol{0}, \tag{2.9}$$

and surface inextensibility along the membrane demands that

$$\boldsymbol{\nabla}_s \cdot \boldsymbol{u}|_S = \hat{\boldsymbol{s}}\left(\hat{\boldsymbol{s}} \cdot \boldsymbol{\nabla}\right) \cdot \boldsymbol{u}|_S = \boldsymbol{0}, \tag{2.10}$$

where $\boldsymbol{\nabla}_s$ is the surface del operator.

2.3. *Force and moment balance*

The membrane is modelled as a thin linearly elastic shell. The bending moment is approximated by $\boldsymbol{M} = B(s)(H - \tilde{H}(s))\hat{\boldsymbol{x}} \times \hat{\boldsymbol{y}}$, where $B(s)$ and $\tilde{H}(s)$ are the spatially varying bending stiffness and spontaneous curvature, and $H = \hat{\boldsymbol{s}} \cdot \partial_s\hat{\boldsymbol{n}}$ is the mean curvature. Force and moment balance along the membrane surface at arclength s are given by $\mathrm{d}\boldsymbol{M}/\mathrm{d}s + \hat{\boldsymbol{s}} \times \boldsymbol{F} = \boldsymbol{0}$ and $\boldsymbol{f}_{elastic} + \boldsymbol{f} = \boldsymbol{0}$, where $\boldsymbol{M}$ is a thickness-averaged first moment of the elastic stress with units of force, $\boldsymbol{f}_{elastic}$ is the elastic force per area of the membrane on a surrounding medium, with $\boldsymbol{f}_{elastic} = \mathrm{d}\boldsymbol{F}/\mathrm{d}s$, and $\boldsymbol{f}$ is the viscous traction

acting on the membrane, (2.7). Defining the tangential component of $\boldsymbol{F}$ as $T(s)$ (the tension per unit length), we then have

$$\boldsymbol{F}(s) = T(s)\hat{\boldsymbol{s}} - \hat{\boldsymbol{s}} \times \left(\frac{\mathrm{d}}{\mathrm{d}s} \left(B(s)(H - \tilde{H}(s)) \right) \hat{\boldsymbol{z}} \right) = T(s)\hat{\boldsymbol{s}} + \hat{\boldsymbol{n}} \left(B(H - \tilde{H}) \right)_s, \tag{2.11}$$

and the elastic force acting on the surrounding medium is then given by

$$\boldsymbol{f}_{elastic} = \left(-TH + \left(B(H - \tilde{H}) \right)_{ss} \right) \hat{\boldsymbol{n}} + \left(T_s + H \left(B(H - \tilde{H}) \right)_s \right) \hat{\boldsymbol{s}}, \tag{2.12}$$

where subscripts indicate partial derivatives. A different expression for the traction appears in the literature starting with the Helfrich free energy which amounts to adding a term $B(s)(H - \tilde{H}(s))^2/2$ to T above (Guckenberger & Gekle 2017); see also the review articles by Powers (2010) and Deserno (2015). In either case T plays the mathematical role of a Lagrange multiplier which assures instantaneous membrane inextensibility, at every moment taking whatever form is necessary to enforce this constraint.

2.4. *Non-dimensionalization*

A competition of viscous and elastic effects emerges when the stresses associated with the flow, the material property variations and the shape deformations are all on the same scale. In order to see this more clearly, the system is made dimensionless by scaling lengths by a, velocities by $a\dot{\gamma}$, forces by $\mu^+ a^2 \dot{\gamma}$, stresses by $\mu^+ \dot{\gamma}$ and energies by $\mu^+ a^3 \dot{\gamma}$, while time is scaled upon $\varepsilon/\dot{\gamma}$. The remaining dimensionless scalar parameters governing the system are

$$R_A = \frac{A}{\pi a^2}, \quad \lambda = \frac{\mu^-}{\mu^+}, \quad \tilde{H}_0 = a\langle \tilde{H}(s) \rangle, \quad Ca = \frac{\mu^+ a^3 \dot{\gamma}}{\langle B(s) \rangle}, \quad \mathcal{C} = \frac{Ca}{\varepsilon}, \tag{2.13a–e}$$

where R_A is the reduced area, λ is the inner/outer viscosity ratio, $\tilde{H}_0$ is the mean spontaneous curvature (with $\langle \cdot \rangle$ an average over the membrane perimeter), Ca is the bending capillary number and $\mathcal{C}$ is a parameter which is $O(1)$ as $\varepsilon \to 0$. In addition to these scalar parameters, and with variations away from their mean values assumed to be small, we have the dimensionless distributions of the bending stiffness and spontaneous curvature along the membrane surface as

$$\frac{B(s(\theta), t)}{\langle B(s) \rangle} = 1 + \varepsilon \kappa(\theta, t), \quad a\tilde{H}(s(\theta), t) = \tilde{H}_0 + \varepsilon \zeta(\theta, t), \tag{2.14a,b}$$

respectively. Like the membrane shape we represent $\kappa(\theta, t)$ by its Fourier series, $\kappa(\theta, t) = \sum_{n=1}^{\infty} c_n(t) \cos(n\theta) + d_n(t) \sin(n\theta)$, and $\zeta(\theta, t)$ similarly with coefficients $e_n(t)$ and $f_n(t)$. Henceforth all variables are understood to be dimensionless.

For a membrane of length $2\pi a \approx 120$ μm and bending rigidity $B \approx 20 k_b T$, with k_b the Boltzmann constant, as measured for a vesicle composed of dioleoylphosphatidylcholine (DOPC) lipids (Dahl *et al.* 2016; Faizi *et al.* 2020), and using the viscosity of water, $\mu^+ \approx 10^{-3}$ Pa s, the bending capillary number Ca is roughly $100\,\dot{\gamma}$[1 s] (e.g. if $\dot{\gamma} = 10^{-1}$ s^{-1} then $Ca \approx 10$). The experimental work of Baumgart *et al.* (2005), where the bending rigidity ratio is approximately 1.25, corresponds here to $\|\varepsilon\kappa\|_\infty \approx 0.1$. The capillary number is highly sensitive to the size; for instance, using a length more appropriate to modelling a red blood cell, $2\pi a \approx 20$ μm, and with $B \approx 50 k_b T$ (Evans 1983), then $Ca \approx \dot{\gamma}/4$. We proceed with the understanding that all variables are now dimensionless. The dimensionless background flow, for instance, is given by $\boldsymbol{u} = y\hat{\boldsymbol{x}}$, and the dimensionless membrane perimeter is $L = 2\pi$.

2.5. *Membrane shape dynamics*

In order to compute the dynamics of the membrane shape, the traction balance is carried out order by order in ε, included as Appendix B, and the tension so found is used instantaneously to solve for the stream function, included as Appendix C. To summarize the results, expansions are written for the pressure, $p = p^{(0)} + \varepsilon p^{(1)} + \ldots$, tension $T = T^{(0)} + \varepsilon T^{(1)} + \ldots$ and velocity $\boldsymbol{u} = u_n\hat{\boldsymbol{n}} + u_s\hat{\boldsymbol{s}} = (u_n^{(1)} + \varepsilon u_n^{(2)} + \ldots)\hat{\boldsymbol{n}} + (u_s^{(1)} + \varepsilon u_s^{(2)} + \ldots)\hat{\boldsymbol{s}}$. The normal and tangential components of the velocity are given at leading order by

$$u_n|_S = \frac{1}{(1+\lambda)}\sin(2\theta) - 2\sum_{n=2}^{\infty} n\left(A_n\cos(n\theta) + B_n\sin(n\theta)\right) + O(\varepsilon), \tag{2.15}$$

$$u_s|_S = -\frac{1}{2} + \frac{1}{2(1+\lambda)}\cos(2\theta) - 2\sum_{n=2}^{\infty}\left(B_n\cos(n\theta) - A_n\sin(n\theta)\right) + O(\varepsilon), \tag{2.16}$$

where

$$A_n = \frac{\mathcal{C}^{-1}\left[\alpha_n(t)a_n + (1-\tilde{H}_0)c_n - e_n\right]}{4(1+\lambda)}, \quad B_n = \frac{\mathcal{C}^{-1}\left[\alpha_n(t)b_n + (1-\tilde{H}_0)d_n - f_n\right]}{4(1+\lambda)}. \tag{2.17a,b}$$

Here we have used the Fourier coefficients for the variations in shape given by a_n, b_n, in bending stiffness by c_n, d_n, and in spontaneous curvature by e_n, f_n, and that $\mathcal{C} = Ca/\varepsilon = O(1)$ as $\varepsilon \to 0$, and have defined

$$\alpha_n(t) = \mathcal{C}\,P_0(t) + n^2 - 1. \tag{2.18}$$

The function $P_0(t)$ is the leading-order mean pressure jump across the membrane, or equivalently the scaled mean tension, (the two are bound together by an elastic analogue of the Young–Laplace law) and is given by

$$P_0(t) = \frac{14b_2 - \mathcal{C}^{-1}\displaystyle\sum_{n=2}^{\infty} n(2n^2-1)C_n}{\displaystyle\sum_{n=2}^{\infty} n(2n^2-1)({a_n}^2 + {b_n}^2)}, \tag{2.19}$$

where

$$C_n = (n^2-1)({a_n}^2 + {b_n}^2) + (1-\tilde{H}_0)\left(a_nc_n + b_nd_n\right) - \left(a_ne_n + b_nf_n\right). \tag{2.20}$$

Note that $n = 2$ terms are present inside the summations in (2.15), (2.16) and (2.19).

Finally, the dynamics of the membrane shape is found using the normal component of the velocity field along the surface. As derived in Appendix D, the shape functions satisfy

$$\rho_t = u_n^{(1)}\Big|_S = \psi_\theta^{(1)}\Big|_{r=1}, \tag{2.21}$$

$$\rho_t^{(2)} = u_n^{(2)}\Big|_S = \psi_\theta^{(2)} + \rho\left(\psi_{r\theta}^{(1)} - \psi_\theta^{(1)}\right) + \rho_\theta\psi_r^{(1)}\Big|_{r=1}, \tag{2.22}$$

with no ambiguity about the stream function (internal or external) owing to the continuity of velocity, (2.9). The end result is that the Fourier modes describing the membrane shape

at first order in ε evolve according to

$$\frac{\mathrm{d}a_n}{\mathrm{d}t} = \frac{n\mathcal{C}^{-1}}{2(1+\lambda)}\left(-\alpha_n(t)a_n + (\tilde{H}_0 - 1)c_n + e_n\right), \tag{2.23}$$

$$\frac{\mathrm{d}b_n}{\mathrm{d}t} = \frac{\delta_{n2}}{1+\lambda} + \frac{n\mathcal{C}^{-1}}{2(1+\lambda)}\left(-\alpha_n(t)b_n + (\tilde{H}_0 - 1)d_n + f_n\right), \tag{2.24}$$

where $\alpha_n(t)$ is given in (2.18), and δ_{n2} is unity when $n = 2$ and is zero otherwise. In addition, $a_1(t) = a_1(0)$ and $b_1(t) = b_1(0)$, which represents that the system is insensitive to translations of the membrane in either direction at first order in ε (the body translates along with the background flow with any vertical perturbation but the shape dynamics is unchanged). The $n = 2$ mode is special since this corresponds to elongation along the principal direction of the background shear flow, at an angle $\pi/4$ relative to the x-axis.

Since $P_0(t)$ depends on the membrane shape, the expressions above are immediately nonlinear, even when only considering the leading-order shape dynamics in small ε. If the mean spontaneous curvature is unity ($\tilde{H}_0 = 1$) the membrane remains close enough to its preferred state at first order in ε so that no additional forces are induced by bending, and only spontaneous curvature variations affect the shape dynamics. For any other mean spontaneous curvature ($\tilde{H}_0 \neq 1$), however, the effects of spontaneous curvature are mathematically indistinguishable from bending stiffness at leading order via (2.23)–(2.24). For the remainder of the paper, we will assume zero spontaneous curvature ($e_n = f_n = 0$ for all n, and $\tilde{H}_0 = 0$), but all of the results to come can be viewed as owing to variations to spontaneous curvature rather than bending stiffness, or any combination thereof.

3. Dynamics of a membrane with uniform material properties

We begin by studying the dynamics of a membrane with uniform bending stiffness ($c_n = d_n = 0$ for all n, and zero spontaneous curvature). In the steady (moving) state, since a_n and b_n are constant in time, the pressure jump $P_0(t)$ in (2.19) is also constant in time. The dynamics in (2.23)–(2.24) then reveals that all Fourier components vanish exponentially fast with the exception of b_2, leaving the steady shape function $\rho(\theta, t) = \tilde{b}_2 \sin(2\theta)$, with $\tilde{b}_2$ easily determined using area conservation alone:

$$\varepsilon\tilde{b}_2 = \varepsilon Q = (2/3)^{1/2}(1 - R_A)^{1/2}. \tag{3.1}$$

Here R_A is the reduced area, having referenced (2.4) when only b_2 is non-zero.

In particular, a membrane with an initial shape of the form $\rho(\theta, 0) = b\sin(2\theta)$ is instantly in a steady state for any b at first order in ε. This corresponds to a tilt angle of $\pi/4$ between the vesicle's elongated axis and the direction of flow. Although the shape is stationary, material is still moving along the tangential direction in a so-called tank-treading motion. In this configuration, the steady-state pressure jump is given by $P_0 = -3\mathcal{C}^{-1} + \tilde{b}_2^{-1}$.

Since the bending stiffness is uniform, we are able to examine the steady shape and orientation to higher order in ε. Assuming that the membrane shape has already relaxed to the point that $u_n^{(1)} = 0$, and hence $\rho_t = 0$ from (2.21), a straight-forward continuation of the regular asymptotic expansion yields equations describing the fluid flow at second

order resulting in the normal velocity on the membrane surface

$$u_n^{(2)} = \tilde{b}_2 \cos(2\theta) - \frac{3\tilde{b}_2^2}{2(1+\lambda)}\left(7\mathcal{C}^{-1} + \tilde{b}_2^{-1}\right)\cos(4\theta) - \frac{1}{2(1+\lambda)}\sum_{n=2}^{\infty} n\left((n^2-4)\mathcal{C}^{-1} + \tilde{b}_2^{-1}\right)\left(a_n^{(2)}\cos(n\theta) + b_n^{(2)}\sin(n\theta)\right). \quad (3.2)$$

(Note that there are $\cos(2\theta)$ and $\cos(4\theta)$ terms inside the infinite sum.) The steady state at second order is reached once $u_n^{(2)} = 0$:

$$\lim_{t\to\infty} \rho^{(2)}(\theta, t) = \tilde{a}_0^{(2)} + \tilde{a}_2^{(2)}\cos(2\theta) + \tilde{a}_4^{(2)}\cos(4\theta), \quad (3.3)$$

where

$$\tilde{a}_0^{(2)} = -(\tilde{b}_2)^2, \quad \tilde{a}_2^{(2)} = (1+\lambda)(\tilde{b}_2)^2, \quad (3.4a,b)$$

$$\tilde{a}_4^{(2)} = -\frac{3(\tilde{b}_2)^2}{4}\left([1 + 7\tilde{b}_2\mathcal{C}^{-1}]/[1 + 12\tilde{b}_2\mathcal{C}^{-1}]\right), \quad (3.5)$$

with $\tilde{b}_2$ given in (3.1). Although we assumed above that $\mathcal{C} = O(1)$ as $\varepsilon \to 0$, the limit of infinite capillary number matches the results of Zahalak, Rao & Sutera (1987) who assumed zero bending stiffness. That the zero-bending-stiffness limit is recovered as $\mathcal{C} \to \infty$ likely identifies this as a regular limit and not a singular one, though a more general analysis for arbitrary $\mathcal{C}$ would be needed to make this result rigorous.

3.1. *Steady-state deformation and inclination angle*

The deformation parameter and orientation angle are two common metrics used to characterize the dynamics of a membrane in flow. The Taylor deformation parameter is defined as $D = (L_1 - L_2)/(L_1 + L_2)$, where $2L_1$ and $2L_2$ are the major and minor axis lengths of an ellipse which shares the same inertia tensor, derived in Appendix E, resulting as $\varepsilon \to 0$ in the representation

$$D(t) = \varepsilon\sqrt{a_2^2 + b_2^2} + \varepsilon^2\left(a_2^{(2)}a_2 + b_2^{(2)}b_2\right)/(\sqrt{a_2^2 + b_2^2}) + O(\varepsilon^3). \quad (3.6)$$

For the case of uniform bending stiffness in the tank-treading steady state,

$$D = \varepsilon\tilde{b}_2 + O(\varepsilon^3) = \sqrt{2(1 - R_A)/3} + O(\varepsilon^3), \quad (3.7)$$

which is notably independent of any other physics in the problem. The eigenvectors of the inertia tensor, meanwhile, are used to define an inclination angle, ϕ, the angle between the elongated axis of the membrane and the direction of flow, which has representation (see Appendix E)

$$\phi(t) = \arctan\left(\frac{-a_2 + \sqrt{a_2^2 + b_2^2}}{b_2}\right) + \varepsilon\frac{\left(b_2^{(2)}a_2 - a_2^{(2)}b_2\right)}{2\left(a_2^2 + b_2^2\right)} + O(\varepsilon^2). \quad (3.8)$$

In the case of uniform bending stiffness, in the steady state we find the angle

$$\phi = \frac{\pi}{4} - \frac{\varepsilon(1+\lambda)}{2}\tilde{b}_2 + O(\varepsilon^2) = \frac{\pi}{4} - (1+\lambda)\sqrt{(1 - R_A)/6} + O(\varepsilon^2), \quad (3.9)$$

consistent with the theory of Finken *et al.* (2008) for $\varepsilon \ll 1$. The predictions above are plotted in figure 2 as lines for a range of reduced areas R_A.

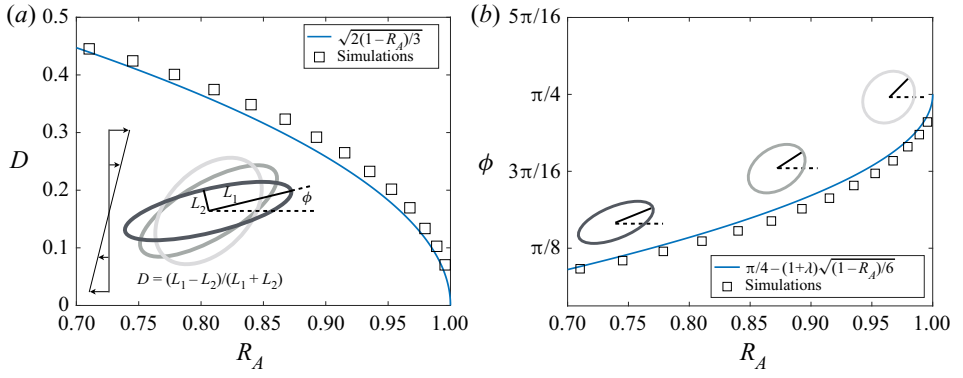

Figure 2. The steady-state deformation parameter (a) and inclination angle (b) in the case of constant bending stiffness with viscosity ratio $\lambda = 1$ and ε varying from 0 to 0.15. Simulations (symbols) and analysis (lines) are in close agreement even for highly deformed membranes.

For nearly circular membranes, the inclination angle approaches $\pi/4$. When fluid is removed from the interior of the membrane, the inclination angle decreases and the membrane tilts forward towards the direction of flow. An increase in the viscosity ratio $\lambda = \mu^-/\mu^+$ further tilts the membrane down towards the direction of flow. From (3.9) the critical value of the viscosity ratio for which the steady inclination angle is equal to zero scales as $1/(1 - R_A)^{1/2}$ as $R_A \to 1$. Beyond this critical viscosity ratio the membrane shape is no longer fixed in space and instead undergoes periodic tumbling. The result is independent of the capillary number, so the same result has been observed in previous work that assumes zero bending rigidity (Zahalak *et al.* 1987) and elsewhere with constant bending stiffness (Finken *et al.* 2008). The result also qualitatively matches the dynamics of a membrane in three dimensions studied by Vlahovska & Gracia (2007), where the inclination angle was also found to be independent of bending rigidity in the small-deformation regime.

To assess the validity of the asymptotic approximations derived above, we solve the complete fluid-structure interaction problem numerically. The incompressible Navier–Stokes equations (which limit to the Stokes equations in (2.8) as the Reynolds number tends to zero) are solved at Reynolds number 10^{-3} on a regular grid using a projection method (Kolahdouz & Salac 2015) and the vesicle is represented using a semi-implicit level set scheme (Osher & Fedkiw 2002). A generalized minimal residual algorithm (GMRES) with algebraic multigrid as provided by the Portable, Extensible Toolkit for Scientific Computation (PETSc) library (Balay *et al.* 2012, 2018, 1997) is used for the level-set solver. Derivatives of the level sets are also tracked, in a so-called 'jet'-scheme, to improve the accuracy of interpolants needed to communicate information from the membrane to the fluid and vice versa (Nave, Rosales & Seibold 2010; Seibold, Rosales & Nave 2012). More details on the numerical methods used and a convergence study for the code are available in the literature (Velmurugan, Kolahdouz & Salac 2016; Gera & Salac 2018*a*).

Figure 2 includes the results of the full simulations (symbols). The steady-state deformation parameter and inclination angle both show excellent agreement with the numerical simulations (and the predicted order of accuracy as $\varepsilon \to 0$, not shown), providing fortuitous accuracy even for substantial membrane deformations where the asymptotic approximations are not immediately expected to hold. The slight overestimate of the deformation parameter for general ε is accompanied by a slight underestimate of

the inclination angle, owing to the higher velocities sampled by a more elongated vesicle. In general, the transition between tank-treading and tumbling can depend weakly on the bending capillary number, which the above analysis suggests enters at the next order in ε (Lebedev *et al.* 2007; Noguchi 2010; Zhao & Shaqfeh 2011).

4. Dynamics of a membrane with variable material properties

If the membrane composition is not uniform, the advection of material around the surface can contribute substantially to the membrane dynamics. Again owing to the mathematically similar contributions of bending stiffness and spontaneous curvature variation we focus our attention on bending stiffness variations. Since the bending stiffness and its spatial variation, κ, are assumed to be material quantities, they evolve in time according to a surface advection equation which is coupled to the shape equations, introducing a serious analytical challenge. For the sake of tractability, however, we assume that mode mixing is small and treat κ as simply advecting by the mean tangential velocity $-1/2$ in (2.16). We will see that this approximation leads to predictions that match very well with the results of full numerical simulations. With the bending stiffness variation confined to a single mode M with amplitude $\bar{\kappa}$ (assumed positive), we thus write

$$\kappa(\theta, t) = \bar{\kappa}\cos\left(M(\theta + \varepsilon t/2)\right) = c_M(t)\cos(M\theta) + d_M(t)\sin(M\theta), \tag{4.1}$$

where $c_M(t) = \bar{\kappa}\cos(\varepsilon M t/2)$ and $d_M(t) = -\bar{\kappa}\sin(\varepsilon M t/2)$. The shape equations are still those in (2.23)–(2.24), with c_m and d_m also now appearing in (2.19). The cases $M = 2$ and $M \neq 2$ are of distinctly different character, and we now proceed to consider them independently.

4.1. *A bifurcation in the dynamic case, $M = 2$*

The situation in which the bending stiffness variation is present in the second spatial mode (i.e. two stiff domains, as in figure 1) is a special case, as this is where the distribution of material properties most strongly interacts with the elongating deformation induced by the flow. From (2.23)–(2.24) the shape dynamics in the second mode evolve according to

$$\frac{\mathrm{d}a_2}{\mathrm{d}t} = \frac{\mathcal{C}^{-1}}{1+\lambda}\left(-\alpha_2(t)a_2 - \bar{\kappa}\cos(\varepsilon t)\right), \tag{4.2}$$

$$\frac{\mathrm{d}b_2}{\mathrm{d}t} = \frac{1}{1+\lambda} + \frac{\mathcal{C}^{-1}}{1+\lambda}\left(\alpha_2(t)b_2 + \bar{\kappa}\sin(\varepsilon t)\right), \tag{4.3}$$

where $\alpha_2(t) = 3 + \mathcal{C}P_0(t)$. Inserting $P_0(t)$, or equivalently solving for $\alpha_2(t)$ so that $\mathrm{d}(a_2^2 + b_2^2)/\mathrm{d}t = \mathrm{d}(Q^2)/\mathrm{d}t = 0$, the above simplify to

$$\frac{\mathrm{d}a_2}{\mathrm{d}t} = -\eta(a_2, b_2, t)b_2, \quad \frac{\mathrm{d}b_2}{\mathrm{d}t} = \eta(a_2, b_2, t)a_2, \tag{4.4a,b}$$

where

$$\eta(a_2, b_2, t) = (1+\lambda)^{-1}Q^{-2}\left[\left(1 + \bar{\kappa}\mathcal{C}^{-1}\sin(\varepsilon t)\right)a_2 + \bar{\kappa}\mathcal{C}^{-1}\cos(\varepsilon t)b_2\right]. \tag{4.5}$$

Recall that Q is a constant which is set at $t = 0$; if the initial shape deformation resides only in the second Fourier mode, for instance, then $Q = (a_2(0)^2 + b_2(0)^2)^{1/2}$. At first order in ε there is no change in the deformation parameter: $D(t) = (2/3)^{1/2}(1 - R_A)^{1/2} + O(\varepsilon^2)$, so the observed shape does not exhibit large variations in time. The inclination

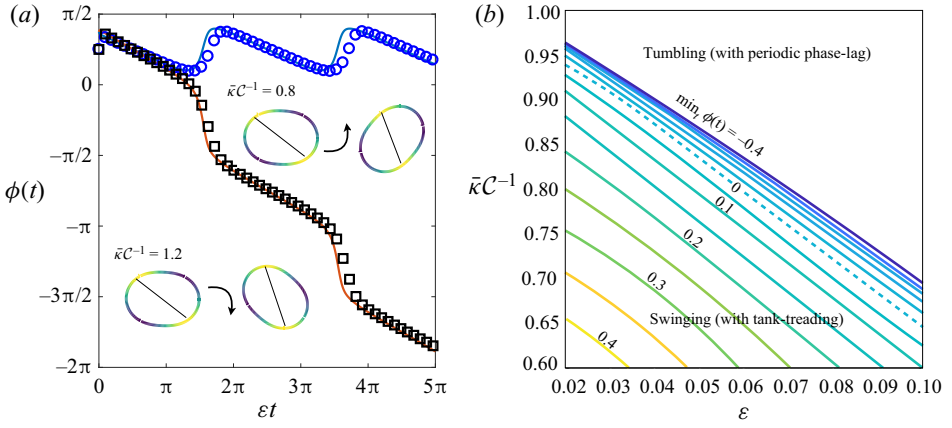

Figure 3. (*a*) The inclination angle as a function of time from simulations (symbols) and theory (lines), with $\varepsilon = 10^{-2}$, $Q = 3$, or $R_A = 0.998$ and $\lambda = 1$. Swinging is observed for $\bar{\kappa}\mathcal{C}^{-1} = 0.8$, tumbling for $\kappa = 1.2$. Both include additional tank-treading motion, indicated by lines in the snapshots – see also figure 4 and supplementary movies M1–M3. (b) Contours of the minimum inclination angle during periodic orbits, $\min_t \phi(t)$, computed using the full numerical simulations. Note that $\bar{\kappa}\mathcal{C}^{-1} = \varepsilon\bar{\kappa}Ca^{-1}$ so that the vertical axis also depends on ε.

angle, however, reveals something striking. Writing $(a_2, b_2) = Q(\cos 2\phi^{(0)}, \sin 2\phi^{(0)})$ (the inclination angle is given by $\phi = \phi^{(0)} + O(\varepsilon)$) and inserting into (4.4*a*,*b*), an equation for $\phi^{(0)}$ arises:

$$\phi_t^{(0)} = \beta\left(\cos(2\phi^{(0)}) + \bar{\kappa}\mathcal{C}^{-1}\sin(2\phi^{(0)} + \varepsilon t)\right), \tag{4.6}$$

with $\beta = (1+\lambda)^{-1}Q^{-1}$. This equation is more constructively analysed by defining the slower time scale $\tau = \varepsilon t$, so that

$$\varepsilon\phi_\tau^{(0)} = \beta\left(\cos(2\phi^{(0)}) + \bar{\kappa}\mathcal{C}^{-1}\sin(2\phi^{(0)} + \tau)\right). \tag{4.7}$$

Numerical solutions of (4.7) for $\bar{\kappa}\mathcal{C}^{-1} = 0.8$ and $\bar{\kappa}\mathcal{C}^{-1} = 1.2$ are shown as lines in figure 3(*a*), for $\varepsilon = 10^{-2}$, $\lambda = 1$ and $Q = 3$. The dynamics alternate between a slow linear drift of $\phi^{(0)}(\tau)$ where $\phi_\tau^{(0)} = O(1)$ and a rapid departure when $\phi^{(0)}$ is near zero. Figure 4, along with supplementary movies M1–M3 available at https://doi.org/10.1017/jfm.2022.40, show the complex dynamics associated with these plots. When $\bar{\kappa}\mathcal{C}^{-1} = 0.8$, the elongated axis swings back and forth relative to the direction of flow; when $\bar{\kappa}\mathcal{C}^{-1} = 1.2$, the shape slowly nears a zero inclination angle, then undergoes a rapid tumble. Also shown in figure 3(*a*) as symbols are the results found using the full numerical simulations, as in § 3, showing close agreement with the solutions generated by (4.7).

When $\bar{\kappa}\mathcal{C}^{-1}$ is small, the bending stiffness variation only introduces a periodic perturbation of the constant bending stiffness dynamics. Linearizing (4.7) about $\phi^{(0)} = \pi/4$, for small $\bar{\kappa}\mathcal{C}^{-1}$ we arrive at the periodic solution

$$\phi^{(0)}(\tau) = \frac{\pi}{4} + \frac{\bar{\kappa}}{2\mathcal{C}}\cos(\tau) + O\left(\left(\bar{\kappa}\mathcal{C}^{-1}\right)^2, \varepsilon\right) \quad \text{as } \bar{\kappa}\mathcal{C}^{-1} \to 0, \tag{4.8}$$

whose period, $\Delta\tau = 2\pi$ (or $\Delta t = 2\pi/\varepsilon$), is twice that of the material's tangential motion along the surface (since the mean surface tangential velocity is $-\varepsilon/2$), owing naturally to the number (two) of stiffer domains. Material tank-treads tangentially along the membrane

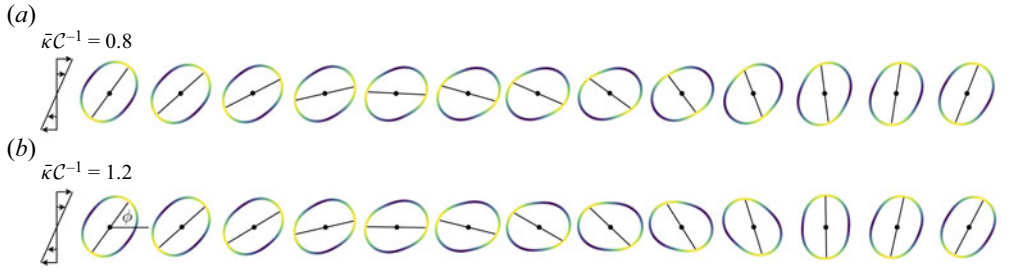

Figure 4. Snapshots of the dynamics associated with figure 3(*a*): swinging with tank-treading ($\bar{\kappa}\mathcal{C}^{-1} = 0.8$, *a*) and tumbling with phase-lagging ($\bar{\kappa}\mathcal{C}^{-1} = 1.2$, *b*) with variable bending stiffness in the $M = 2$ mode. A line in each snapshot connects the two softer regions, which are lighter in colour than the darker, stiffer regions. The vesicle elongates so that the softer regions tend to sit in large curvature regions, while the principal direction of the background flow stretches the vesicle towards inclination angle $\pi/4$. See also supplementary movies M1–M3.

while the shape swings back and forth. The rapid slipping in figure 3(*a*) for the smaller $\bar{\kappa}\mathcal{C}^{-1}$ value occurs when the stiffer material passes quickly over the region of highest curvature.

For very large values of $\bar{\kappa}\mathcal{C}^{-1}$, the dynamics limit to a pure (rigid-body) tumbling motion. Assuming a regular perturbation expansion in small $\mathcal{C}/\bar{\kappa}$, the inclination angle has the asymptotic behaviour

$$\phi^{(0)}(\tau) = \frac{\pi}{2} - \frac{\tau}{2} - \frac{\mathcal{C}}{4\bar{\kappa}}\left(2\cos(\tau) - \varepsilon(1+\lambda)Q\right) + O\left((\mathcal{C}/\bar{\kappa})^2, \varepsilon^2\right) \quad \text{as } \bar{\kappa}\mathcal{C}^{-1} \to \infty, \tag{4.9}$$

with all other parameters assumed $O(1)$. When $\bar{\kappa}\mathcal{C}^{-1}$ is finite, the tumbling motion is joined by a small relative tangential material oscillation. This periodic phase-lag of the material becomes more pronounced as $\bar{\kappa}\mathcal{C}^{-1}$ is reduced closer to unity, and vanishes as $\bar{\kappa}\mathcal{C}^{-1} \to \infty$, leading ultimately to pure (rigid-body) tumbling motion.

For a given material property contrast, we have now seen that decreasing the shear rate below a critical value produces, perhaps counter-intuitively, a tumbling motion, while increasing it above this value invites the vesicle to swing. With a very slow background flow, the vesicle elongates in the directions of its softest components (or higher spontaneous curvature regions) in a quasi-steady manner – the material is nearly matched to the shape as it rotates like a rigid body. But in a flow with a large shear rate, material is driven around the surface with larger viscous stresses relative to the elastic stresses, and the stiffer material may be driven past the high curvature regions. High curvature regions can rapidly align with the softer regions via a rapid swing.

Similar transitions from swinging to tumbling have been observed in red blood cells (Noguchi 2009), capsules (Kessler, Finken & Seifert 2008; Barthes-Biesel 1991, 2016) and vesicles even with uniform bending rigidity (Kantsler & Steinberg 2006; Lebedev *et al.* 2007; Deschamps *et al.* 2009*a*,*b*) but at smaller reduced areas. In addition, the variation in spontaneous curvature along the surface of a red blood cell has previously been modelled through a simple energy barrier – there too the contrast in material properties revealed a transition from tumbling to swinging (Skotheim & Secomb 2007). More directly, Vlahovska *et al.* (2011) investigated the dynamics of microcapsules of non-spherical reference shape in shear flow, much like the specification of a non-uniform spontaneous curvature. In their fully three-dimensional treatment they too observed tumbling to swinging behaviour upon increasing the shear rate beyond a critical value.

4.1.1. *Matched asymptotic analysis*

Between these two extremes lies a critical value of $\bar{\kappa}\mathcal{C}^{-1}$ which signals a bifurcation from swinging to tumbling. Figure 3(*b*) shows the minimum inclination angle achieved during the periodic dynamics for a range of ε and $\bar{\kappa}\mathcal{C}^{-1}$ found using the full numerical simulations. The bending stiffness variation needed to set off a tumbling dynamics is near unity as $\varepsilon \to 0$ (consistent with the much simpler numerical solutions of (4.7)) and is a decreasing function of ε. Note that $\bar{\kappa}\mathcal{C}^{-1} = \varepsilon\bar{\kappa}Ca^{-1}$ depends on ε in figure 3(*b*). A thin band near this bifurcation ridge shows an unexpected result: the membrane's inclination angle can decrease to values less than zero even during a (rather dramatic) swinging motion. Common intuition from single-component membrane dynamics suggests that once the elongated axis has dipped below the x-axis the membrane will surely tumble; this intuition is thus not always correct.

We are therefore led to investigate the regime where $\bar{\kappa}\mathcal{C}^{-1} = 1 + O(\varepsilon)$ and we define $\alpha = (\bar{\kappa}\mathcal{C}^{-1} - 1)/\varepsilon$ with $\alpha = O(1)$ as $\varepsilon \to 0$. For values of τ where $\phi^{(0)}_\tau = O(1)$ as $\varepsilon \to 0$, the inclination angle is drifting slowly and an outer solution is derived assuming a regular expansion in ε, $\phi^{(0)} = \phi^{(0)}_{outer} + O(\varepsilon)$, resulting in $\phi^{(0)}_{outer}(\tau) = 3\pi/8 - \tau/4 + O(\varepsilon)$. The initial value of $\phi^{(0)}$ does not appear in the outer solution because the distribution of bending stiffness begins entirely in the $\cos(2\theta)$ mode at $\tau = 0$ from (4.1); there is a rapid correction on a time scale $O(\varepsilon)$ (just visible near $\tau = 0$ in figure 3*a*) before the outer solution becomes dominant, and memory of the initial state is almost immediately lost.

An inner region of rapid variation in $\phi^{(0)}$ emerges when $\phi^{(0)} \approx 0$, or when $\tau \approx 3\pi/2$. The scaling of the inner region in τ and the solution there are found by appealing to dominant balance as $\varepsilon \to 0$ (Bender & Orszag 2013), leading to the definition of an inner variable $\sigma = (\tau - 3\pi/2)/\varepsilon^{1/2}$, so that (4.7) reads as

$$\varepsilon^{1/2}\phi^{(0)}_\sigma = \beta\left(\cos\left(2\phi^{(0)}\right) - (1+\varepsilon\alpha)\cos\left(2\phi^{(0)} + \varepsilon^{1/2}\sigma\right)\right), \tag{4.10}$$

where $\beta = (1+\lambda)^{-1}Q^{-1}$, and an ansatz $\phi^{(0)}_{inner} = p^{(0)}_{inner}(\sigma) + \varepsilon^{1/2}p^{(1)}_{inner}(\sigma) + O(\varepsilon)$. At leading order we find

$$\frac{\mathrm{d}}{\mathrm{d}\sigma}p^{(0)}_{inner} = \beta\sigma\,\sin(2p^0_{inner}), \tag{4.11}$$

which has solution

$$p^{(0)}_{inner}(\sigma) = \tan^{-1}\left(C_0 e^{\beta\sigma^2}\right), \tag{4.12}$$

with C_0 an integration constant. However, in order for this inner solution to merge with the outer solution, or

$$\lim_{\tau\to 3\pi/2^-}\phi^{(0)}_{outer} = \lim_{\sigma\to-\infty}\phi^{(0)}_{inner}, \tag{4.13}$$

we must have that $C_0 = 0$. At the next order (4.10) then produces

$$\frac{\mathrm{d}}{\mathrm{d}\sigma}p^{(1)}_{inner} = \beta\left(\alpha - \frac{\sigma^2}{2} - 2\sigma p^{(1)}_{inner}\right), \tag{4.14}$$

and the solution

$$p^{(1)}_{inner}(\sigma) = -\frac{\sigma}{4} + \Upsilon\left(\mathrm{erf}(\beta^{1/2}\sigma) + C_1\right)\mathrm{e}^{\beta\sigma^2}, \tag{4.15}$$

where C_1 is an integration constant and

$$\Upsilon = \frac{1}{8}\left(\frac{\pi}{\beta}\right)^{1/2}(1 - 4\beta\alpha). \tag{4.16}$$

The error function, $\mathrm{erf}(\beta^{1/2}\sigma) = (2/\sqrt{\pi})\int_0^{\beta^{1/2}\sigma} \mathrm{e}^{-t^2}\,\mathrm{d}t$, is an odd function which tends towards -1 as $\sigma \to -\infty$ and to 1 as $\sigma \to \infty$. Again the requirement of matching to the outer solution demands that terms which are unbounded as $\sigma \to -\infty$ vanish, leading to $C_1 = 1$. The inner solution alone then represents a composite approximation for $\tau \in (O(\varepsilon), 3\pi/2]$:

$$\phi^{(0)}(\tau) \sim \frac{3\pi}{8} - \frac{\tau}{4} + \varepsilon^{1/2}\Upsilon\left[\mathrm{erf}\left(\sqrt{\frac{\beta}{\varepsilon}}\left(\tau - \frac{3\pi}{2}\right)\right) + 1\right]\exp(\beta(\tau - 3\pi/2)^2/\varepsilon). \tag{4.17}$$

This solution becomes unbounded when τ increases beyond $3\pi/2$, so is incapable of merging with the possible outer solutions to the right of $\tau = 3\pi/2$, either $7\pi/8 - \tau/4$ if $(1 - 4\beta\alpha) > 0$ (a swing) or $-\pi/8 - \tau/4$ if $(1 - 4\beta\alpha) < 0$ (a tumble). Instead we continue the solution by solving (4.7) on $\tau \geqslant 3\pi/2$ using the initial data from the inner solution above, $\phi^{(0)}(3\pi/2) = \varepsilon^{1/2}\Upsilon + O(\varepsilon)$.

The solution at leading order is again that in (4.12) but this time $C_0 \neq 0$. After finding the solution at the next order (included as Appendix F), however, in order to match both the data at $\tau = 3\pi/2$ and to merge with an outer solution it becomes clear that $C_0 = O(\varepsilon^{1/2})$, and then the equation for $p^{(1)}_{inner}$ in (4.14) and its general solution in (4.15) go unchanged. Removing unbounded terms as $\sigma \to \infty$ selects $C_1 = -1$, and matching the data at $\tau = 3\pi/2$ selects $C_0 = \tan(2\varepsilon^{1/2}\Upsilon)$, resulting in the following composite solution for $\tau \in [3\pi/2, 3\pi/2 + 2\pi - O(\varepsilon^{1/2}))$:

$$\begin{aligned}\phi^{(0)}(\tau) \sim \frac{3\pi}{8} - \frac{\tau}{4} + \tan^{-1}\left[\tan\left(2\varepsilon^{1/2}\Upsilon\right)\exp(\beta(\tau - 3\pi/2)/\varepsilon)\right] \\ + \varepsilon^{1/2}\Upsilon\left[\mathrm{erf}\left(\sqrt{\frac{\beta}{\varepsilon}}\left(\tau - \frac{3\pi}{2}\right)\right) - 1\right]\exp(\beta(\tau - 3\pi/2)^2/\varepsilon).\end{aligned} \tag{4.18}$$

The critical dependence of the dynamics on the sign of $\bar{\kappa}\mathcal{C}^{-1} - 1$ as $\varepsilon \to 0$ is thus established, most clearly through the dependence of the argument of $\tan^{-1}$ on the sign of Υ, and thus on the sign of $(1 - 4\beta\alpha)$ (and recalling that $\alpha = (\bar{\kappa}\mathcal{C}^{-1} - 1)/\varepsilon$).

Since $\beta > 0$, if $\bar{\kappa}\mathcal{C}^{-1} < 1$ then $(1 - 4\beta\alpha) > 0$ and the solution above shows a rapid return to a positive inclination angle just less than $\pi/2$, representing a dramatic swinging motion. If $\bar{\kappa}\mathcal{C}^{-1} > 1$, however, then the dynamics depend on $\beta = [(1 + \lambda)Q]^{-1}$. If $\beta > 1/(4\alpha)$, then $(1 - 4\beta\alpha) < 0$ and as τ increases beyond $3\pi/2$ the inclination angle dips rapidly towards negative values and below $-\pi/2$, representing a tumble. If $\beta < 1/(4\alpha)$, however, the inclination angle becomes negative as τ increases away from $3\pi/2$ for a short while, but then for longer times it launches back towards positive values: in this case the membrane's long axis dips below the horizontal, hinting at a tumble, but then rapidly pulls back up into positive inclination angles in a high-amplitude swing. Inclination angles from numerical solution of (4.6) with $\varepsilon = 10^{-2}$ are plotted for a range of $\bar{\kappa}\mathcal{C}^{-1}$ in figure 5. The approximations in (4.17)–(4.18) are visibly indistinguishable (and not shown) from numerical solution of (4.6) in this parameter regime.

The inclination angle equation, (4.6), only provides a solution for the $O(1)$ behaviour of the inclination angle, $\phi^{(0)}(t)$, so while the expressions above are accurate asymptotic solutions to (4.6), the equation itself is only representing the $O(1)$ behaviour of the inclination angle $\phi(t)$. While these analytical representations show remarkable accuracy when compared to the full numerical simulations, seen in figure 3(*a*), certain aspects of the full system are delicate. For instance, the analysis above suggests that the critical

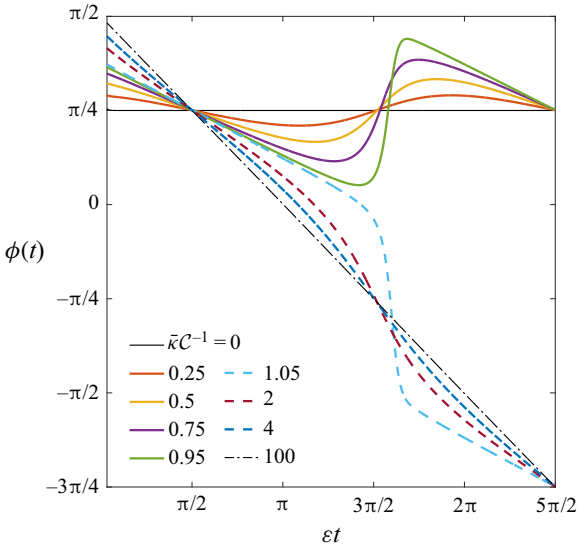

Figure 5. Theoretical inclination angle (solutions of (4.6)) with spatial period $M = 2$ of material property variation, viscosity ratio $\lambda = \mu^-/\mu^+ = 1$, $\varepsilon = 10^{-2}$ or $R_A = 0.998$, and $Q = 3$ for a range of $\bar{\kappa}\mathcal{C}^{-1}$.

$\bar{\kappa}\mathcal{C}^{-1}$ beyond which tumbling occurs is an increasing function of ε, but this lies in stark contrast to the results of the full numerical simulations shown in figure 3(*b*). The analysis above shows, however, that the critical value for the onset of tumbling is indeed $\bar{\kappa}\mathcal{C}^{-1} = 1 + O(\varepsilon)$ as $\varepsilon \to 0$, and generally provides accurate dynamics in a very wide variety of settings.

4.2. *The case $M \neq 2$*

Turning now to the case where $M \neq 2$, the daunting system is rendered harmless upon observation of a periodic steady state in which $P_0(t)$ is constant. According to (2.23)–(2.24) with P_0 assumed constant, as $t \to \infty$ we find $a_n = 0$ and $b_n = 0$ for all $n \notin \{2, M\}$. Meanwhile, as in the constant bending stiffness case, b_2 relaxes to an equilibrium value $\tilde{b}_2$, where $\tilde{b}_2 = \mathcal{C}/\alpha_2 = \mathcal{C}(3 + \mathcal{C}\,P_0)^{-1}$.

Shape deformations continue periodically in the Mth Fourier mode, however, according to (2.23)–(2.24) (upon inserting $c_M(t)$ and $d_M(t)$ from (4.1)). At leading order in ε the system is quasi-steady; with $\tau = \varepsilon t$ again, we write $\partial_t a_M = \varepsilon \partial_\tau a_M$ (similarly for b_M). Neglecting a transient relaxation from initial data, to leading order in small ε we find

$$a_M(t) = \frac{-\bar{\kappa}}{\alpha_M} \cos\left(\frac{M\varepsilon t}{2}\right), \quad b_M(t) = \frac{\bar{\kappa}}{\alpha_M} \sin\left(\frac{M\varepsilon t}{2}\right). \tag{4.19a,b}$$

Simply, then, in the periodic steady state we have $a_M^2 + b_M^2 = \bar{\kappa}^2/\alpha_M^2$ and $a_M c_M + b_M d_M = -\bar{\kappa}^2/\alpha_M$. As both are constant, along with the constant value of b_2 in the limit as $t \to \infty$, upon inspection of P_0 in (2.19) we verify the consistency of this result: P_0 is indeed constant in this periodic steady state. Since $\tilde{b}_2$ is determined purely by the constraint of constant area, from (3.1), the pressure jump P_0 associated with these dynamics is the same as that in the constant bending case. Moreover, the deformation parameter and inclination angle in the $M \neq 2$ case are also unchanged. The membrane

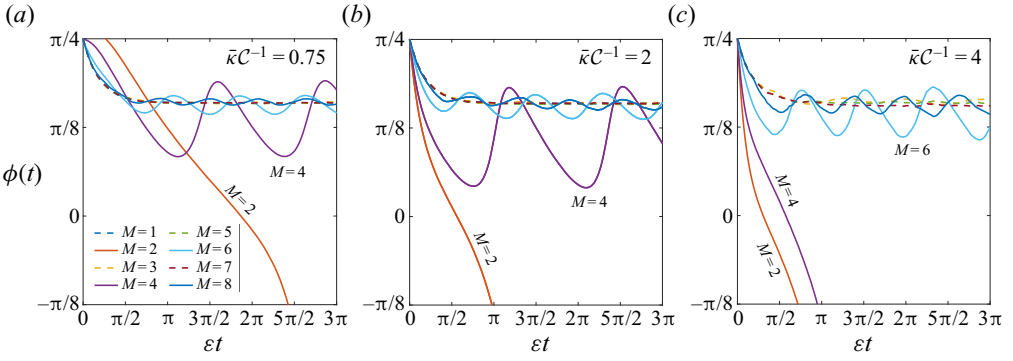

Figure 6. Inclination angle dynamics with bending stiffness variations in the Mth spatial mode for $M \in \{1, 2, \ldots, 8\}$ with $\varepsilon = 0.1$ or $R_A = 0.865$ and $\lambda = 1$ for three variation amplitudes, from the full numerical simulations. (*a*) $\bar{\kappa}\mathcal{C}^{-1} = 0.75$, (*b*) $\bar{\kappa}\mathcal{C}^{-1} = 2$ and (*c*) $\bar{\kappa}\mathcal{C}^{-1} = 4$. Tumbling is observed in small, even modes. (See also supplementary movies M4–M6.)

simply elongates in the direction of the principle axis of the straining flow while shape oscillations in the Mth mode traverse along this constant background geometry in a trembling dynamics.

When $\bar{\kappa}\mathcal{C}^{-1}$ is sufficiently large, interactions between the modes of bending stiffness can no longer be neglected (i.e. our simple specification of $\kappa(\theta)$ in (4.1) becomes inaccurate). Full numerical simulations are used to explore this challenging region of parameter space. Figure 6 shows the inclination angles computed using the full numerical simulations for $M \in \{1, 2, \ldots, 8\}$, with $\varepsilon = 0.1$ and $\lambda = 1$ fixed, for three different bending stiffness variations: $\bar{\kappa}\mathcal{C}^{-1} = 0.75$, $\bar{\kappa}\mathcal{C}^{-1} = 2$ and $\bar{\kappa}\mathcal{C}^{-1} = 4$. The $M = 2$ mode results in tumbling in all three cases, consistent with figure 3(*b*). The swinging amplitude with even M values increases with increasing $\bar{\kappa}\mathcal{C}^{-1}$, however, and the $M = 4$ case transitions from swinging to tumbling for some $\bar{\kappa}\mathcal{C}^{-1} \in (2, 4)$. Supplementary movies M4–M6 show the dynamics of vesicles with $M \in \{1, 2, \ldots, 8\}$ represented in figure 6(*a–c*).

In the simulated dynamics, we observe membrane swinging for small, even M, but not odd M, or large even M with an insufficiently large value of $\bar{\kappa}\mathcal{C}^{-1}$. When M is even, the two regions of largest curvature have a symmetric interaction with the membrane, and elongation in the direction of the softer material reduces the energy at both ends. Bending stiffness information in the $M = 4$, mode, for instance, bleeds into the $M = 2$ mode, which interacts directly with the extensional part of the background flow and can lead to tumbling, as discussed in the previous section. When M is odd, however, the large curvature regions have an asymmetric interaction with the membrane; reorientation of the elongated axis which would reduce the bending energy on one end would increase it on the other end. Finally, when M is large, either even or odd, averaging results in convergence to the case of constant bending stiffness, and departures from the inclination angle chosen by the principal axis of the background flow, $\pi/4$ as $\varepsilon \to 0$, become negligible. It remains to be seen whether a sufficiently large $\bar{\kappa}\mathcal{C}^{-1}$ can result in tumbling for any even M; extremely stiff regions do not pass easily across high curvature regions, suggesting that tumbling might ensue for very large values of $\bar{\kappa}\mathcal{C}^{-1}$, but high spatial frequency averaging suggests convergence to pure tank-treading as in § 3. The answer may well depend on the reduced area and viscosity ratio. We leave this intriguing question for future inquiry.

5. Discussion

The material property variations along the surface of a multicomponent vesicle can impact the vesicle dynamics in a background flow differently depending on the spatial modes of its distribution, the magnitude of those variations and even the parity of the number of domains. Small amplitude variations in material properties lead to periodic oscillations of a pure tank-treading steady state about an inclination angle of $\pi/4$; large variations can result in a rigid-body tumbling mode with a constant rotation rate; and an intermediate regime shows a bifurcation from swinging with tank-treading to tumbling with periodic material phase-lag. As the membrane becomes more deflated, the critical value of $\bar{\kappa}\mathcal{C}^{-1}$ required for the vesicle to tumble is found to decrease, with $\bar{\kappa}\mathcal{C}^{-1}$ approaching 1 as ε approaches 0. As a general principle, the vesicle has a tendency to elongate so that the softer parts of the membrane sit in the regions of largest curvature, while the background flow tends to elongate the vesicle along the principal axis with a fixed inclination angle of $\pi/4$. When these two directions are not aligned, swinging, or even tumbling, ensues. That the capillary number is highly sensitive to the vesicle size may be of use to experimental realizations of the results described in this paper.

Although we have focused on variations in bending stiffness, at leading order we find the same shapes, dynamics and bifurcation from swinging to tumbling when considering variations in spontaneous curvature instead. Equations (2.23)–(2.24) indicate that when the preferred mean curvature along the membrane, $\tilde{H}_0$, is not unity, the effects of bending stiffness variations and spontaneous curvature variations are indistinguishable for each Fourier mode. A model linking the two (e.g. if bending stiffness is proportional to spontaneous curvature for a given lipid species) may then be necessary to make claims about material properties in full using this passive means of probing membrane composition. If $\tilde{H}_0 = 1$, however, then only spontaneous curvature variations enter at first order in ε.

Replacing bending stiffness by spontaneous curvature, if $\tilde{H}_0 = 0$, the transition between tumbling and swinging for the $M = 2$ spatial mode is predicted at the critical value $a[\tilde{H}]\mathcal{C}^{-1} = 1$ as $\varepsilon \to 0$, with $[\tilde{H}]$ the curvature contrast. Estimating the spontaneous curvature variations of a red blood cell to be roughly $[\tilde{H}] = 0.5\ \mu\text{m}^{-1}$ with $a \approx 3\ \mu\text{m}$, and with $Ca \approx \dot{\gamma}/4$ from § 2.4, the theoretical prediction is that the bifurcation should appear near $\dot{\gamma} \approx 2\ \text{s}^{-1}$. This is very close to the shear rates used in experiments showing the onset of this transition (Abkarian, Faivre & Viallat 2007; Abkarian & Viallat 2008).

In the fully three-dimensional system, material domains are not confined to motion in the flow direction only and this may result in a substantial departure from the results described herein in certain regimes. Particularly when slow motions yield to sudden reorganization, as in a rapid swing or tumbling event, the addition of such an escape direction may prove critical. But some material properties cannot so easily be disturbed, for instance, the spontaneous curvature of a red blood cell provided by the scaffolding of its spectrin network (Dao, Lim & Suresh 2003; Hatami-Marbini & Mofrad 2015). That the transition from tumbling to swinging in red blood cells appears to be predicted already using this two-dimensional analysis, however, is intriguing.

The distribution of membrane domains is of substantial biological importance. Membrane heterogeneity can impact fundamental cellular functions such as signal transduction and membrane trafficking (Simons & Toomre 2000; Maxfield 2002; Edidin 2003), and improper composition can cause diseases such as Alzheimer's (Vetrivel & Thinakaran 2010; Rajendran & Annaert 2012). The predictions of this work suggests a means of determining not only the constant material properties of a membrane or vesicle using a background flow, which has been an experimentally viable method for decades, but

now also of determining material property variations by linking time-series dynamics to spatial material variations, and even the possibility of using a simple pressure probe near such a swinging, tumbling and trembling membrane. With good fortune, these predictions will be of use for measuring heterogeneous membrane properties using only viscous stresses in the near future.

Supplementary movies. Supplementary movies are available at https://doi.org/10.1017/jfm.2022.40.

Funding. S.E.S. acknowledges the support of the NSF/NIH (DMS-1661900, DMR-2003819).

Declaration of interests. The authors report no conflict of interest.

Author ORCIDs.
Prerna Gera https://orcid.org/0000-0001-8365-2626;
David Salac https://orcid.org/0000-0002-6151-8247;
Saverio E. Spagnolie https://orcid.org/0000-0002-8484-1573.

Appendix A. Stream function and incompressibility in polar coordinates

The (dimensional) biharmonic equation in polar coordinates (r, θ) has a general solution known as the Michell solution (Michell 1899). Neglecting terms which are non-periodic in θ, the biharmonic equations inside $(-)$ and outside $(+)$ the vesicle are solved by

$$\begin{aligned}\psi^{\pm} = {} & A_0^{\pm} r^2 + B_0^{\pm} r^2 \ln(r) + C_0^{\pm} \ln(r) + \left(A_1^{\pm} r + B_1^{\pm} r^{-1} + C_1^{\pm} r^3 + D_1^{\pm} r \ln(r)\right) \cos(\theta) \\ & + \left(E_1^{\pm} r + F_1^{\pm} r^{-1} + G_1^{\pm} r^3 + H_1^{\pm} r \ln(r)\right) \sin(\theta) \\ & + \sum_{n=2}^{\infty} \left(A_n^{\pm} r^n + B_n^{\pm} r^{-n} + C_n^{\pm} r^{n+2} + D_n^{\pm} r^{2-n}\right) \cos(n\theta) \\ & + \sum_{n=2}^{\infty} \left(E_n^{\pm} r^n + F_n^{\pm} r^{-n} + G_n^{\pm} r^{n+2} + H_n^{\pm} r^{2-n}\right) \sin(n\theta). \end{aligned} \tag{A1}$$

The coefficients above are determined instantaneously in time by demanding that ψ^- and its derivatives are bounded at the origin, convergence to the far-field limit ($\psi^+ \to \dot{\gamma} r^2 \sin^2(\theta)/2$ as $r \to \infty$), continuity of velocity across the membrane boundary, $[\nabla \psi]_S = \mathbf{0}$, traction balance (see Appendix B), and surface inextensibility along the membrane, $\nabla_s \cdot \boldsymbol{u}|_S = 0$, where ∇_s is the surface del operator,

$$\begin{aligned}\nabla_s = \hat{\boldsymbol{s}} \left(\hat{\boldsymbol{s}} \cdot \nabla\right) &= \left(\hat{\boldsymbol{\theta}} + \varepsilon \rho_\theta \hat{\boldsymbol{r}} + O(\varepsilon^2)\right) \left(\hat{\boldsymbol{\theta}} + \varepsilon \rho_\theta \hat{\boldsymbol{r}} + O(\varepsilon^2)\right) \cdot \left(\hat{\boldsymbol{r}} \partial_r + \hat{\boldsymbol{\theta}} \frac{1}{r} \partial_\theta\right) \\ &= \hat{\boldsymbol{\theta}} \frac{1}{r} \partial_\theta + \varepsilon \left(\hat{\boldsymbol{\theta}} \rho_\theta \partial_r + \hat{\boldsymbol{r}} \frac{\rho_\theta}{r} \partial_\theta\right) + O(\varepsilon^2). \end{aligned} \tag{A2}$$

Inextensibility is given in terms of the radial and azimuthal velocity components u_r and u_θ by

$$\nabla_s \cdot \boldsymbol{u}|_S = \nabla_s \cdot \left(u_r \hat{\boldsymbol{r}} + u_\theta \hat{\boldsymbol{\theta}}\right)\Big|_S = \frac{1}{r} \left(\partial_\theta u_\theta + u_r\right)\Big|_{r=1} + O(\varepsilon |\boldsymbol{u}|) = 0. \tag{A3}$$

In terms of the stream function, the relations $u_r = \psi_\theta / r$ and $u_\theta = -\psi_r$ are inserted into the above to give

$$\nabla_s \cdot \boldsymbol{u}|_S = \frac{1}{r}\left(-\partial_{r\theta}\psi + \frac{1}{r}\partial_\theta \psi\right)\bigg|_{r=1} + O(\varepsilon\psi) = 0. \tag{A4}$$

More terms above are kept to extend the approximation to higher order.

Appendix B. Traction balance asymptotics

Traction balance is demanded order by order in the small parameter ε. Regular perturbation expansions for the (dimensionless) stream function, $\psi = \psi^{(1)} + \varepsilon\psi^{(2)} + \ldots$, pressure $p = p^{(0)} + \varepsilon p^{(1)} + \varepsilon^2 p^{(2)} + \ldots$ and viscous traction $\boldsymbol{f} = \boldsymbol{f}^{(0)} + \varepsilon \boldsymbol{f}^{(1)} + \ldots$ are assumed. The dimensionless viscous traction is given at leading order (from (2.7)) by $\boldsymbol{f}^{(0)} = -[p^{(0)}]\hat{\boldsymbol{n}}$, and the contribution at first order in ε is given by

$$\begin{aligned}\boldsymbol{f}^{(1)} = &-\left([p^{(1)} + \rho(\theta,t)\partial_r p^{(0)}] + 2[\partial_\theta \psi^{(1)} - \partial_{r\theta}\psi^{(1)}]^{(\lambda)}\right)\hat{\boldsymbol{n}} \\ &+ [\partial_{\theta\theta}\psi^{(1)} + \partial_r \psi^{(1)} - \partial_{rr}\psi^{(1)}]^{(\lambda)}\hat{\boldsymbol{s}},\end{aligned} \tag{B1}$$

where we have defined a jump operator which incorporates the viscosity ratio,

$$[\psi]^{(\lambda)} = \psi^+ - \lambda\psi^-\big|_S. \tag{B2}$$

This viscous traction must balance with the elastic traction. At leading order, traction balance in the tangential and normal directions returns

$$\partial_\theta T^{(0)} = 0, \tag{B3}$$

$$-T^{(0)} - [p^{(0)}] = 0. \tag{B4}$$

Hence, $T^{(0)} = -[p^{(0)}] =: P_0(t)$; the leading-order isotropic tension is balanced with the leading-order pressure jump across the interface, a dimensionless statement of an elastic Young–Laplace law. At the next order in ε, traction balance in the tangential and normal directions are given by

$$\partial_\theta T^{(1)} - \mathcal{C}^{-1}\left((\tilde{H}_0 - 1)\partial_\theta \kappa + \partial_\theta \zeta + \partial_\theta^3 \rho + \partial_\theta \rho\right) + [\partial_{\theta\theta}\psi^{(1)} + \partial_r\psi^{(1)} - \partial_{rr}\psi^{(1)}]^{(\lambda)} = 0, \tag{B5}$$

with $\mathcal{C} = Ca/\varepsilon$ defined in (2.13*a–e*), κ and ζ the first-order material property variations defined in (2.14*a*,*b*), and

$$\begin{aligned}&-T^{(1)} + \left(\rho + \partial_\theta^2 \rho\right)P_0 - \mathcal{C}^{-1}\left((\tilde{H}\tilde{H}_0 - 1)\partial_\theta^2 \kappa + \partial_\theta^2 \zeta + \partial_\theta^4 \rho + \partial_\theta^2 \rho\right) \\ &\quad - \left([p^{(1)} + \rho(\theta,t)\partial_r p^{(0)}] + 2[\partial_\theta \psi^{(1)} - \partial_{r\theta}\psi^{(1)}]^{(\lambda)}\right) = 0.\end{aligned} \tag{B6}$$

In the limit of infinite bending capillary number (i.e. zero bending stiffness) these expressions are consistent with those provided by Zahalak *et al.* (1987). The membrane length and area constraints, enforced out to second order in ε as $\varepsilon \to 0$, are used to determine pressure jump at the interface P_0 at leading order (or the isotropic tension $T^{(0)}$), leading to the expression in (2.19).

Appendix C. First-order solution

Equations (2.8), (2.9), (2.10), (B5) and (B6) are solved simultaneously for the dimensionless first-order stream function $\psi^{(1)}$ (via (A1), properly scaled) and pressure $p^{(1)}$ both inside and outside the vesicle, and for the first-order membrane tension, $T^{(1)}$. The resulting stream functions are given by

$$\psi^{(1)-} = \frac{r^2}{4} - \frac{r^2(3-r^2)}{4(1+\lambda)}\cos(2\theta) + \sum_{n=2}^{\infty} r^n \left((n+1) - (n-1)r^2\right)(B_n\cos(n\theta) - A_n\sin(n\theta)) \tag{C1}$$

and

$$\psi^{(1)+} = \frac{r^2}{4} - \left(\frac{\lambda + r^2(1-2\lambda) + r^4(1+\lambda)}{4r^2(1+\lambda)}\right)\cos(2\theta) + \sum_{n=2}^{\infty}\left((n+1)r^{2-n} - (n-1)r^{-n}\right)(B_n\cos(n\theta) - A_n\sin(n\theta)) \tag{C2}$$

(note that $n = 2$ terms are also in the summation), where A_n, B_n are given in (2.17*a*,*b*). With $p^{(0)+} = p_\infty$ and $p^{(0)-} = p_\infty + P_0$ the (spatially constant) leading-order pressure fields, with P_0 given in (2.19), the first-order pressure fields are

$$p^{(1)-} = \Pi - \frac{3\lambda r^2}{1+\lambda}\sin(2\theta) + 4\lambda\sum_{n=2}^{\infty}(n^2-1)r^n\,(B_n\sin(n\theta) + A_n\cos(n\theta)) \tag{C3}$$

and

$$p^{(1)+} = \frac{(2\lambda-1)}{r^2(1+\lambda)}\sin(2\theta) + 4\sum_{n=2}^{\infty} r^{-n}(n^2-1)\,(B_n\sin(n\theta) - A_n\cos(n\theta))\,, \tag{C4}$$

where Π is a constant. Finally, the membrane tension at first order is given by

$$T^{(1)} = \Pi - \sin(2\theta) - \sum_{n=1}^{\infty}(4(1+\lambda)B_n - P_0 b_n)\sin(n\theta) + (4(1+\lambda)A_n - P_0 a_n)\cos(n\theta). \tag{C5}$$

The free constant Π appears in both $p^{(1)-}$ and $T^{(1)}$, indicating an ambiguity which is understood upon interpretation of the pressure and tension fields as Lagrange multipliers which enforce fluid and membrane incompressibility and inextensibility, respectively, and recalling that the two are linked by the Young–Laplace law. The value of Π has no bearing on the dynamics.

Appendix D. From the stream function to the surface velocity

For a given station in arclength s, the no-slip condition is written as $\partial_t \boldsymbol{r}(s,t) = \boldsymbol{u}(\boldsymbol{r}(s,t),t)$; to focus on fixed values of θ we write $\boldsymbol{r}(s,t) = \boldsymbol{r}(s(\theta,t),t) = r(\theta,t)\hat{\boldsymbol{r}}(\theta)$. Then noting that

$$\left.\frac{\partial \boldsymbol{r}}{\partial t}\right|_s = \frac{\mathrm{d}\boldsymbol{r}}{\mathrm{d}t} - \frac{\partial \boldsymbol{r}}{\partial s}\frac{\partial s}{\partial t}\bigg|_\theta = \frac{\mathrm{d}\boldsymbol{r}}{\mathrm{d}t} - \hat{\boldsymbol{s}}\left.\frac{\partial s}{\partial t}\right|_\theta, \tag{D1}$$

dotting with the normal vector removes the need to determine $\partial_t s$ for fixed θ:

$$\hat{\boldsymbol{n}} \cdot \frac{\partial \boldsymbol{r}}{\partial t} = \hat{\boldsymbol{n}} \cdot \frac{\mathrm{d}\boldsymbol{r}}{\mathrm{d}t} = \hat{\boldsymbol{n}} \cdot \boldsymbol{u}\big|_S, \tag{D2}$$

and thus $\partial_t(r(\theta,t)\hat{\boldsymbol{r}}) \cdot \hat{\boldsymbol{n}} = \hat{\boldsymbol{n}} \cdot \boldsymbol{u}|_S$. Then with $\boldsymbol{u} = u_n\hat{\boldsymbol{n}} + u_s\hat{\boldsymbol{s}} = u_r\hat{\boldsymbol{r}} + u_\theta\hat{\boldsymbol{\theta}}$, and all dimensionless velocities expanded as $\boldsymbol{u} = \boldsymbol{u}^{(1)} + \varepsilon\boldsymbol{u}^{(2)} + \ldots$,

$$\frac{\mathrm{d}}{\mathrm{d}t}\left(r(\theta,t)\hat{\boldsymbol{r}}\right) \cdot \hat{\boldsymbol{n}} = \left(\varepsilon\rho_t + \varepsilon^2\rho_t^{(2)} + O(\varepsilon^3)\right)\left(1 + O(\varepsilon^2)\right) = \varepsilon\rho_t + \varepsilon^2\rho_t^{(2)} + O(\varepsilon^3) \tag{D3}$$

and

$$\hat{\boldsymbol{n}} \cdot \boldsymbol{u}\big|_S = \left(\hat{\boldsymbol{r}} - \varepsilon\rho_\theta\hat{\boldsymbol{\theta}} + O(\varepsilon^2)\right) \cdot \boldsymbol{u}\Big|_S = \left(u_r^{(1)} + \varepsilon\left(u_r^{(2)} - \rho_\theta u_\theta^{(1)}\right) + O(\varepsilon^2)\right)\Big|_S. \tag{D4}$$

Recall that the dimensional velocity is scaled by $\dot{\gamma}$, so that a dimensionless velocity $\boldsymbol{u}^{(1)}$ which is $O(1)$ as $\varepsilon \to 0$ corresponds to a dimensional velocity $\dot{\gamma}\boldsymbol{u}^{(1)}$ which is $O(\varepsilon)$ as $\varepsilon \to 0$. Since the velocities in the radial and azimuthal directions are given by

$$u_r|_S = \frac{1}{r}\psi_\theta(r,\theta)\bigg|_{r=1+\varepsilon\rho+O(\varepsilon^2)} = \psi_\theta^{(1)}\Big|_{r=1} + \varepsilon\left(\psi_\theta^{(2)} + \rho\left(\psi_{r\theta}^{(1)} - \psi_\theta^{(1)}\right)\right)\Big|_{r=1} + O(\varepsilon^2), \tag{D5}$$

$$u_\theta|_S = -\psi_r(r,\theta)|_{r=1+\varepsilon\rho+O(\varepsilon^2)} = -\psi_r^{(1)}\Big|_{r=1} - \varepsilon\left(\psi_r^{(2)} + \rho\psi_{rr}^{(1)}\right)\Big|_{r=1} + O(\varepsilon^2), \tag{D6}$$

the velocity in the surface normal direction may be written as

$$\hat{\boldsymbol{n}} \cdot \boldsymbol{u}\big|_S = \psi_\theta^{(1)}\Big|_{r=1} + \varepsilon\left(\psi_\theta^{(2)} + \rho(\psi_{r\theta}^{(1)} - \psi_\theta^{(1)}) + \rho_\theta\psi_r^{(1)}\right)\Big|_{r=1} + O(\varepsilon^2). \tag{D7}$$

Hence, since the dimensional time is scaled by $\varepsilon/\dot{\gamma}$,

$$\rho_t = u_n^{(1)}\Big|_S = u_r^{(1)}\Big|_S = \psi_\theta^{(1)}\Big|_{r=1} \tag{D8}$$

and

$$\rho_t^{(2)} = u_n^{(2)}\Big|_S = u_r^{(2)} - \rho_\theta u_\theta^{(1)}\Big|_S = \psi_\theta^{(2)} + \rho\left(\psi_{r\theta}^{(1)} - \psi_\theta^{(1)}\right) + \rho_\theta\psi_r^{(1)}\Big|_{r=1}. \tag{D9}$$

Since the gradient of the stream function is continuous across the membrane boundary, either ψ^+ or ψ^- may be inserted into the above without ambiguity. Using the results of Appendix C, the normal and tangential components of the velocity are then given by (2.15)–(2.16).

Appendix E. Inertia tensor, deformation parameter and inclination angle

The deformation parameter, $D = (L_1 - L_2)/(L_1 + L_2)$, is defined using the axis lengths $2L_1$ and $2L_2$ of the ellipse which shares the same inertia tensor. With Ω denoting the vesicle's interior, the inertia tensor is defined as

$$\mathbb{I} = \int_\Omega \begin{pmatrix} y^2 & -xy \\ -xy & x^2 \end{pmatrix} \mathrm{d}x\,\mathrm{d}y. \tag{E1}$$

When Ω is the interior of an ellipse with major and minor axis lengths $2L_1$ and $2L_2$, respectively, oriented with its major axis at an angle θ relative to the x-axis, this

tensor has eigenvalues $\lambda_1 = \pi L_1^3 L_2/4$ and $\lambda_2 = \pi L_1 L_2^3/4$, with associated eigenvectors $\boldsymbol{v}_1 = (\sin^2\theta, -\sin(2\theta)/2)$ and $\boldsymbol{v}_2 = (\cos^2\theta, \sin(2\theta)/2)$. In terms of the eigenvalues of the inertia tensor, then, $L_1 = (4/\pi)^{1/4}(\lambda_1^3/\lambda_2)^{1/8}$ and $L_2 = (4/\pi)^{1/4}(\lambda_2^3/\lambda_1)^{1/8}$, the deformation parameter is given by

$$D = \frac{L_1 - L_2}{L_1 + L_2} = \frac{\lambda_1^{1/2} - \lambda_2^{1/2}}{\lambda_1^{1/2} + \lambda_2^{1/2}}, \tag{E2}$$

and the inclination angle may be recovered from $\boldsymbol{v}_2$ via $\theta = \tan^{-1}(\hat{\boldsymbol{y}} \cdot \boldsymbol{v}_2/\hat{\boldsymbol{x}} \cdot \boldsymbol{v}_2)$.

Considering the general membrane boundary S, parameterized as in § 2, the inertia tensor above instead has eigenvalues

$$\lambda_1 = \frac{1}{4}\left\{\pi + 2\pi\varepsilon\sqrt{a_2^2 + b_2^2} + \varepsilon^2\left(3\left(a_2^2 + b_2^2\right) + 2\frac{a_2^{(2)}a_2 + b_2^{(2)}b_2}{\sqrt{a_2^2 + b_2^2}}\right)\right\} + O(\varepsilon^3), \tag{E3}$$

$$\lambda_2 = \frac{1}{4}\left\{\pi - 2\pi\varepsilon\sqrt{a_2^2 + b_2^2} + \varepsilon^2\left(3\left(a_2^2 + b_2^2\right) - 2\frac{a_2^{(2)}a_2 + b_2^{(2)}b_2}{\sqrt{a_2^2 + b_2^2}}\right)\right\} + O(\varepsilon^3), \tag{E4}$$

and then (E2) produces the deformation parameter in (3.6). The eigenvector associated with λ_2 has components

$$\hat{\boldsymbol{x}} \cdot \boldsymbol{v}_2 = b_2^3 + a_2 b_2\left(\sqrt{a_2^2 + b_2^2} + a_2\right) - \varepsilon\left(\sqrt{a_2^2 + b_2^2} + a_2\right)(b_2^{(2)}a_2 - a_2^{(2)}b_2), \tag{E5}$$

$$\hat{\boldsymbol{y}} \cdot \boldsymbol{v}_2 = b_2^2\sqrt{a_2^2 + b_2^2}, \tag{E6}$$

and then $\tan^{-1}(\hat{\boldsymbol{y}} \cdot \boldsymbol{v}_2/\hat{\boldsymbol{x}} \cdot \boldsymbol{v}_2)$ returns the inclination angle in (3.8).

Appendix F. General solution to the inner expansion equations

The general solution to (4.11) is

$$p_{inner}^{(0)}(\sigma) = m\pi + \tan^{-1}\left(C_0\,\mathrm{e}^{\beta\sigma^2}\right), \tag{F1}$$

for m an integer and C_0 an integration constant. At the next order (4.10) then produces

$$\frac{\mathrm{d}}{\mathrm{d}\sigma}p_{inner}^{(1)} = \beta\left(\frac{1 - C_0^2\,\mathrm{e}^{2\beta\sigma^2}}{1 + C_0^2\,\mathrm{e}^{2\beta\sigma^2}}\right)\left(\alpha - \frac{\sigma^2}{2} - 2\sigma p_{inner}^{(1)}\right), \tag{F2}$$

and the solution

$$p_{inner}^{(1)}(\sigma) = \frac{C_1\,\mathrm{e}^{\beta\sigma^2}}{1 + C_0^2\,\mathrm{e}^{2\beta\sigma^2}} - \frac{\sigma}{4} + \frac{\pi^{1/2}\,\mathrm{e}^{\beta\sigma^2}}{8\beta^{1/2}\left(1 + C_0^2\,\mathrm{e}^{2\beta\sigma^2}\right)}\left(C_0^2(1+4\alpha\beta)\mathrm{erfi}\left(\beta^{1/2}\sigma\right) + (1 - 4\alpha\beta)\mathrm{erf}\left(\beta^{1/2}\sigma\right)\right), \tag{F3}$$

where C_1 is an integration constant. The imaginary error function, $\mathrm{erfi}(\beta^{1/2}\sigma) = (2/\sqrt{\pi})\int_0^{\beta^{1/2}\sigma}\mathrm{e}^{t^2}\,\mathrm{d}t$, tends towards $\mathrm{e}^{\beta\sigma^2}/\sqrt{\pi\beta\sigma^2}$ as $|\sigma| \to \infty$.

The approach in § 4.1 requires that $p^{(0)}_{inner}(0) + \varepsilon^{1/2} p^{(1)}_{inner}(0) = \varepsilon^{1/2}\Upsilon + O(\varepsilon)$, with Υ defined in (4.16), resulting in

$$m\pi + \tan^{-1}(C_0) + \frac{\varepsilon^{1/2} C_1}{1 + C_0^2} = \varepsilon^{1/2}\Upsilon + O(\varepsilon). \tag{F4}$$

Here we see that C_0 cannot be $O(1)$ as $\varepsilon \to 0$, as in this case matching the initial data at $\tau = 3\pi/2$ is not possible. But C_0 cannot be zero or else either matching to the data above, or merging with the outer solution as $\sigma \to \infty$, is not possible. The equation above is then to be seen as a signal that C_0 is in fact $O(\varepsilon^{1/2})$ as $\varepsilon \to 0$.

References

Abkarian, M., Faivre, M. & Viallat, A. 2007 Swinging of red blood cells under shear flow. *Phys. Rev. Lett.* **98** (18), 188302.

Abkarian, M. & Viallat, A. 2008 Vesicles and red blood cells in shear flow. *Soft Matt.* **4** (4), 653–657.

Abreu, D., Levant, M., Steinberg, V. & Seifert, U. 2014 Fluid vesicles in flow. *Adv. Colloid Interface Sci.* **208**, 129–141.

Ahmadpoor, F. & Sharma, P. 2016 Thermal fluctuations of vesicles and nonlinear curvature elasticity—implications for size-dependent renormalized bending rigidity and vesicle size distribution. *Soft Matt.* **12** (9), 2523–2536.

Balay, S., *et al.* 2018 PETSc users manual. *Tech. Rep.* ANL-95/11 – Revision 3.9. Argonne National Laboratory.

Balay, S., Brown, F., Buschelman, K., Gropp, W.D., Kaushik, D., Knepley, M.G., McInnes, L.C., Smith, B.F. & Zhang, H. 2012 PETSc web page http://www.mcs.anl.gov/petsc.

Balay, S., Gropp, W.D., McInnes, L.C. & Smith, B.F. 1997 Efficient management of parallelism in object oriented numerical software libraries. In *Modern Software Tools in Scientific Computing* (ed. E. Arge, A.M. Bruaset & H.P. Langtangen), pp. 163–202. Birkhäuser.

Barrett, J.W., Garcke, H. & Nürnberg, R. 2017 Finite element approximation for the dynamics of fluidic two-phase biomembranes. *ESAIM: Math. Model. Numer. Anal.* **51** (6), 2319–2366.

Barthes-Biesel, D. 1980 Motion of a spherical microcapsule freely suspended in a linear shear flow. *J. Fluid Mech.* **100** (4), 831–853.

Barthes-Biesel, D. 1991 Role of interfacial properties on the motion and deformation of capsules in shear flow. *Physica* A **172**, 103–124.

Barthes-Biesel, D. 2016 Motion and deformation of elastic capsules and vesicles in flow. *Annu. Rev. Fluid Mech.* **48**, 25–52.

Barthes-Biesel, D. & Rallison, J.M. 1981 The time-dependent deformation of a capsule freely suspended in a linear shear flow. *J. Fluid Mech.* **113**, 251–267.

Baumgart, T., Das, S., Webb, W.W. & Jenkins, J.T. 2005 Membrane elasticity in giant vesicles with fluid phase coexistence. *Biophys. J.* **89** (2), 1067–1080.

Baumgart, T., Hess, S.T. & Webb, W.W 2003 Imaging coexisting fluid domains in biomembrane models coupling curvature and line tension. *Nature* **425** (6960), 821–824.

Bender, C.M. & Orszag, S.A. 2013 *Advanced Mathematical Methods for Scientists and Engineers I: Asymptotic Methods and Perturbation Theory*. Springer Science & Business Media.

Cox, G. & Lowengrub, J. 2015 The effect of spontaneous curvature on a two-phase vesicle. *Nonlinearity* **28** (3), 773–793.

Dahl, J.B., Narsimhan, V., Gouveia, B., Kumar, S., Shaqfeh, E.S.G. & Muller, S.J. 2016 Experimental observation of the asymmetric instability of intermediate-reduced-volume vesicles in extensional flow. *Soft Matt.* **12** (16), 3787–3796.

Dao, M., Lim, C.T. & Suresh, S. 2003 Mechanics of the human red blood cell deformed by optical tweezers. *J. Mech. Phys. Solids* **51** (11–12), 2259–2280.

Deschamps, J., Kantsler, V., Segre, E & Steinberg, V. 2009*a* Dynamics of a vesicle in general flow. *Proc. Natl Acad. Sci. USA* **106** (28), 11444–11447.

Deschamps, J., Kantsler, V. & Steinberg, V. 2009*b* Phase diagram of single vesicle dynamical states in shear flow. *Phys. Rev. Lett.* **102** (11), 118105.

Deserno, M. 2015 Fluid lipid membranes: from differential geometry to curvature stresses. *Chem. Phys. Lipids* **185**, 11–45.

EDIDIN, M. 2003 The state of lipid rafts: from model membranes to cells. *Annu. Rev. Biophys. Biomol. Struct.* **32** (1), 257–283.

ELLIOTT, C.M. & STINNER, B. 2013 Computation of two-phase biomembranes with phase dependent material parameters using surface finite elements. *Commun. Math. Phys.* **13** (2), 325–360.

ENGELHARDT, H., DUWE, H.P. & SACKMANN, E. 1985 Bilayer bending elasticity measured by Fourier analysis of thermally excited surface undulations of flaccid vesicles. *J. Phys. Lett.* **46** (8), 395–400.

EVANS, E.A. 1983 Bending elastic modulus of red blood cell membrane derived from buckling instability in micropipet aspiration tests. *Biophys. J.* **43** (1), 27–30.

FAIZI, H.A., REEVES, C.J., GEORGIEV, V.N., VLAHOVSKA, P.M. & DIMOVA, R. 2020 Fluctuation spectroscopy of giant unilamellar vesicles using confocal and phase contrast microscopy. *Soft Matt.* **16** (39), 8996–9001.

FINKEN, R., LAMURA, A., SEIFERT, U. & GOMPPER, G. 2008 Two-dimensional fluctuating vesicles in linear shear flow. *Eur. Phys. J.* E **25** (3), 309–321.

FREUND, J.B. 2014 Numerical simulation of flowing blood cells. *Annu. Rev. Fluid Mech.* **46**, 67–95.

GAO, T. & LI, Z. 2017 Self-driven droplet powered by active nematics. *Phys. Rev. Lett.* **119** (10), 108002.

GERA, P. & SALAC, D. 2018*a* Modeling of multicomponent three-dimensional vesicles. *Comput. Fluids* **172**, 362–383.

GERA, P. & SALAC, D. 2018*b* Three-dimensional multicomponent vesicles: dynamics and influence of material properties. *Soft Matt.* **14** (37), 7690–7705.

GUCKENBERGER, A. & GEKLE, S. 2017 Theory and algorithms to compute Helfrich bending forces: a review. *J. Phys.: Condens. Matter* **29** (20), 203001.

HATAMI-MARBINI, H. & MOFRAD, M.R.K. 2015 Rheology and mechanics of the cytoskeleton. In *Complex Fluids in Biological Systems* (ed. S.E. Spagnolie), pp. 187–205. Springer.

HU, J., WEIKL, T. & LIPOWSKY, R. 2011 Vesicles with multiple membrane domains. *Soft Matt.* **7** (13), 6092–6102.

KANTSLER, V., SEGRE, E. & STEINBERG, V. 2008 Dynamics of interacting vesicles and rheology of vesicle suspension in shear flow. *Europhys. Lett.* **82** (5), 58005.

KANTSLER, V. & STEINBERG, V. 2006 Transition to tumbling and two regimes of tumbling motion of a vesicle in shear flow. *Phys. Rev. Lett.* **96** (3), 036001.

KELLER, S.R. & SKALAK, R. 1982 Motion of a tank-treading ellipsoidal particle in a shear-flow. *J. Fluid Mech.* **120**, 27–47.

KESSLER, S., FINKEN, R. & SEIFERT, U. 2008 Swinging and tumbling of elastic capsules in shear flow. *J. Fluid Mech.* **605**, 207–226.

KOLAHDOUZ, E.M. & SALAC, D. 2015 Electrohydrodynamics of three-dimensional vesicles: a numerical approach. *SIAM J. Sci. Comput.* **37** (3), B473–B494.

KUMAR, A. & GRAHAM, M.D. 2015 Cell distribution and segregation phenomena during blood flow. In *Complex Fluids in Biological Systems* (ed. S.E. Spagnolie), pp. 399–435. Springer.

LEBEDEV, V.V., TURITSYN, K.S. & VERGELES, S.S. 2008 Nearly spherical vesicles in an external flow. *New J. Phys.* **10** (4), 043044.

LEBEDEV, V.V., TURITSYN, K.S. & VERGELES, S.S. 2007 Dynamics of nearly spherical vesicles in an external flow. *Phys. Rev. Lett.* **99**, 218101.

LI, S., LOWENGRUB, J. & VOIGT, A. 2012 Locomotion, wrinkling, and budding of a multicomponent vesicle in viscous fluids. *Commun. Math. Sci.* **10** (2), 645–670.

LIU, K., MARPLE, G.R., ALLARD, J., LI, S., VEERAPANENI, S. & LOWENGRUB, J. 2017 Dynamics of a multicomponent vesicle in shear flow. *Soft Matt.* **13** (19), 3521–3531.

LOWENGRUB, J.S., RÄTZ, A. & VOIGT, A. 2009 Phase-field modeling of the dynamics of multicomponent vesicles: spinodal decomposition, coarsening, budding, and fission. *Phys. Rev.* E **79**, 031926.

MARENDUZZO, D. & ORLANDINI, E. 2013 Phase separation dynamics on curved surfaces. *Soft Matt.* **9** (4), 1178–1187.

MAXFIELD, F.R. 2002 Plasma membrane microdomains. *Curr. Opin. Cell Biol.* **14** (4), 483–487.

MICHALET, X., BENSIMON, D. & FOURCADE, B. 1994 Fluctuating vesicles of nonspherical topology. *Phys. Rev. Lett.* **72** (1), 168.

MICHELL, J.H. 1899 On the direct determination of stress in an elastic solid, with application to the theory of plates. *Proc. Lond. Math. Soc.* **1** (1), 100–124.

MISBAH, C. 2006 Vacillating breathing and tumbling of vesicles under shear flow. *Phys. Rev. Lett.* **96** (2), 028104.

MISBAH, C. 2012 Vesicles, capsules and red blood cells under flow. *J. Phys.: Conf. Ser.* **392**, 012005.

MORSE, D.C. & MILNER, S.T. 1994 Fluctuations and phase behavior of fluid membrane vesicles. *Europhys. Lett.* **26** (8), 565.

MUSHENHEIM, P.C., PENDERY, J.S., WEIBEL, D.B., SPAGNOLIE, S.E. & ABBOTT, N.L. 2016 Straining soft colloids in aqueous nematic liquid crystals. *Proc. Natl Acad. Sci. USA* **113** (20), 5564–5569.

NAVE, J.C., ROSALES, R.R. & SEIBOLD, B. 2010 A gradient-augmented level set method with an optimally local, coherent advection scheme. *J. Comput. Phys.* **229** (10), 3802–3827.

NOGUCHI, H. 2009 Swinging and synchronized rotations of red blood cells in simple shear flow. *Phys. Rev.* E **80**, 021902.

NOGUCHI, H. 2010 Dynamics of fluid vesicles in oscillatory shear flow. *J. Phys. Soc. Japan* **79** (2), 024801.

NOGUCHI, H. & GOMPPER, G. 2007 Swinging and tumbling of fluid vesicles in shear flow. *Phys. Rev. Lett.* **98** (12), 128103.

OLLA, P. 2011 Tank-treading as a means of propulsion in viscous shear flows. *J. Fluid Mech.* **680**, 265–286.

OSHER, S.J. & FEDKIW, R.P. 2002 *Level Set Methods and Dynamic Implicit Surfaces*, 1st edn. Springer.

POWERS, T.R. 2010 Dynamics of filaments and membranes in a viscous fluid. *Rev. Mod. Phys.* **82** (2), 1607.

QUAIFE, B., GANNON, A. & YOUNG, Y.-N. 2021 Hydrodynamics of a semipermeable vesicle under flow and confinement. *Phys. Rev. Fluids* **6**, 073601.

RAFFIEE, A.H., DABIRI, S. & ARDEKANI, A.M. 2019 Suspension of deformable particles in Newtonian and viscoelastic fluids in a microchannel. *Microfluid Nanofluid* **23** (2), 22.

RAJENDRAN, L. & ANNAERT, W. 2012 Membrane trafficking pathways in alzheimer's disease. *Traffic* **13** (6), 759–770.

SALAC, D. & MIKSIS, M.J. 2012 Reynolds number effects on lipid vesicles. *J. Fluid Mech.* **711**, 122–146.

SCHNEIDER, M.B., JENKINS, J.T. & WEBB, W.W. 1984 Thermal fluctuations of large quasi-spherical bimolecular phospholipid vesicles. *J. Phys.* **45** (9), 1457–1472.

SEIBOLD, B., ROSALES, R.R. & NAVE, J.C. 2012 Jet schemes for advection problems. *J. Discrete Continuous Dyn. Syst.* **17** (4), 1229–1259.

SEIFERT, U. 1997 Configurations of fluid membranes and vesicles. *Adv. Phys.* **46** (1), 13–137.

SEIFERT, U. 1999 Fluid membranes in hydrodynamic flow fields: formalism and an application to fluctuating quasispherical vesicles in shear flow. *Eur. Phys. J.* B **8** (3), 405–415.

SEOL, Y., TSENG, Y., KIM, Y. & LAI, M. 2019 An immersed boundary method for simulating Newtonian vesicles in viscoelastic fluid. *J. Comput. Phys.* **376**, 1009–1027.

SIMONS, K. & TOOMRE, D. 2000 Lipid rafts and signal transduction. *Nat. Rev. Mol. Cell Biol.* **1** (1), 31–39.

SKOTHEIM, J.M. & SECOMB, T.W 2007 Red blood cells and other nonspherical capsules in shear flow: oscillatory dynamics and the tank-treading-to-tumbling transition. *Phys. Rev. Lett.* **98** (7), 078301.

SMITH, K.A. & USPAL, W.E 2007 Shear-driven release of a bud from a multicomponent vesicle. *J. Chem. Phys.* **126** (7), 02B610.

SOHN, J.S., TSENG, Y.-H., LI, S., VOIGT, A. & LOWENGRUB, J.S. 2010 Dynamics of multicomponent vesicles in a viscous fluid. *J. Comput. Phys.* **229** (1), 119–144.

STANICH, C.A., HONERKAMP-SMITH, A.R., PUTZEL, G.G., WARTH, C.S., LAMPRECHT, A.K., MANDAL, P., MANN, E., HUA, T.D. & KELLER, S.L. 2013 Coarsening dynamics of domains in lipid membranes. *Biophys. J.* **105** (2), 444–454.

TIAN, A., JOHNSON, C., WANG, W. & BAUMGART, T. 2007 Line tension at fluid membrane domain boundaries measured by micropipette aspiration. *Phys. Rev. Lett.* **98** (20), 208102.

TUSCH, S., LOISEAU, E., AL-HALIFA, A., KHELLOUFI, K., HELFER, E. & VIALLAT, A. 2018 When giant vesicles mimic red blood cell dynamics: swinging of two-phase vesicles in shear flow. *Phys. Rev. Fluids* **3** (12), 123605.

VEATCH, S.L. & KELLER, S.L. 2003 Separation of liquid phases in giant vesicles of ternary mixtures of phospholipids and cholesterol. *Biophys. J.* **85** (5), 3074–3083.

VEERAPANENI, S.K., RAHIMIAN, A., BIROS, G. & ZORIN, D. 2011*a* A fast algorithm for simulating vesicle flows in three dimensions. *J. Comput. Phys.* **230** (14), 5610–5634.

VEERAPANENI, S.K., YOUNG, Y.-N., VLAHOVSKA, P.M. & BŁAWZDZIEWICZ, J. 2011*b* Dynamics of a compound vesicle in shear flow. *Phys. Rev. Lett* **106** (15), 158103.

VELMURUGAN, G., KOLAHDOUZ, E.M. & SALAC, D. 2016 Level set jet schemes for stiff advection equations: the SemiJet method. *Comput. Meth. Appl. Mech. Engng* **310**, 233–251.

VETRIVEL, K.S. & THINAKARAN, G. 2010 Membrane rafts in Alzheimer's disease beta-amyloid production. *Biochim. Biophys. Acta: Mol. Cell. Biol. Lipids* **1801** (8), 860–867.

VLAHOVSKA, P.M. & GRACIA, R.S. 2007 Dynamics of a viscous vesicle in linear flows. *Phys. Rev.* E **75** (1), 016313.

VLAHOVSKA, P.M., PODGORSKI, T. & MISBAH, C. 2009 Vesicles and red blood cells in flow: from individual dynamics to rheology. *C. R. Phys.* **10** (8), 775–789.

VLAHOVSKA, P.M., YOUNG, Y.-N., DANKER, G. & MISBAH, C. 2011 Dynamics of a non-spherical microcapsule with incompressible interface in shear flow. *J. Fluid Mech.* **678**, 221–247.

VLAHOVSKA, P.M. 2015 Dynamics of membrane-bound particles: capsules and vesicles. In *Fluid-Structure Interactions in Low-Reynolds-Number Flows* (ed. C. Duprat and H.A. Stone), pp. 313–346.

VLAHOVSKA, P.M. & MISBAH, C. 2019 Theory of vesicle dynamics in flow and electric fields. In *The Giant Vesicle Book* (ed. R. Dimova and C. Marques), pp. 195–210. CRC Press.

WORTIS, M., JARIĆ, M. & SEIFERT, U. 1997 Thermal shape fluctuations of fluid-phase phospholipid-bilayer membranes and vesicles. *J. Mol. Liq.* **71** (2–3), 195–207.

YOUNG, Y.-N., SHELLEY, M.J. & STEIN, D.B. 2021 The many behaviors of deformable active droplets. *Math. Biosci. Engng* **18** (3), 2849–2881.

ZABUSKY, N.J., SEGRE, E., DESCHAMPS, J., KANTSLER, V. & STEINBERG, V. 2011 Dynamics of vesicles in shear and rotational flows: modal dynamics and phase diagram. *Phys. Fluids* **23** (4), 041905.

ZAHALAK, G.I., RAO, P.R. & SUTERA, S.P. 1987 Large deformations of a cylindrical liquid-filled membrane by a viscous shear flow. *J. Fluid Mech.* **179**, 283–305.

ZHAO, H. & SHAQFEH, E.S.G 2011 The dynamics of a vesicle in simple shear flow. *J. Fluid Mech.* **674**, 578–604.

ZHAO, H., SHAQFEH, E.S.G. & NARSIMHAN, V. 2012 Shear-induced particle migration and margination in a cellular suspension. *Phys. Fluids* **24** (1), 011902.

ZHAO, H., SPANN, A.P. & SHAQFEH, E.S.G. 2011 The dynamics of a vesicle in a wall-bound shear flow. *Phys. Fluids* **23** (12), 121901.

ZHAO, Y. & DU, Q. 2011 Diffuse interface model of multicomponent vesicle adhesion and fusion. *Phys. Rev.* E **84** (1), 011903.